

Concordance of X-ray and AlphaFold2 Models of SARS-CoV-2 Main Protease with Residual Dipolar Couplings Measured in Solution

Angus J. Robertson,^a Joseph M. Courtney,^a Yang Shen, Jinfa Ying, and Ad Bax*

Laboratory of Chemical Physics, NIDDK, National Institutes of Health, Bethesda MD,
20892-0520, USA

^a Contributed equally

SUPPORTING INFORMATION

Table of Contents

SI TEXT: RDC SAMPLE PREPARATION	3
SI TEXT: ALPHA FOLD2 IMPLEMENTATION	4
SI TEXT: RDC FITTING REGION BOUNDARY DETERMINATION	5
FIGURE S1: ARTSY-HNCO PULSE SEQUENCE	6
FIGURE S2: TATER PULSE SEQUENCE.....	7
FIGURE S3: CORRELATION BETWEEN $^1D_{NH}$ AND $^2D_{C^H}$ COUPLINGS.....	8
FIGURE S4: MAGNITUDE OF RDC ERROR BY RESIDUE FOR ARTSY-HNCO AND TATER EXPERIMENTS	9
FIGURE S5: PROTONATION METHOD DEPENDENCE OF N-H ^N AND C'-H ^N VECTOR ORIENTATION.....	15
FIGURE S6: RDC RESIDUALS AND DIPOLEAR INTERACTION VECTOR DISTRIBUTIONS ACROSS X-RAY STRUCTURES.....	11
FIGURE S7-S9: EFFECT OF AMBER RELAXATION ON PREDICTED RDCs IN ALPHA FOLD2 MODELS	12
FIGURE S10: EFFECT OF AMBER RELAXATION ON N-H BOND VECTOR ORIENTATIONS	15
FIGURE S11: MAGNITUDE OF N-H BOND VECTOR ORIENTATIONAL CHANGE ON AMBER RELAXATION OF AF2 MODELS.....	16
TABLE S1: DATA COLLECTION AND PROCESSING PARAMETERS.....	17
TABLE S2: EXPERIMENTAL $^1D_{NH}$ AND $^2D_{C^H}$ RDC VALUES.....	18
TABLE S3: FITS OF X-RAY AND ALPHA FOLD2 MODELS TO RDCs	26
TABLE S4: PDB ENTRIES USED BY ALPHA FOLD2 IMPLEMENTATIONS	28
TABLE S5: SEQUENCE SIMILARITY OF TEMPLATE STRUCTURES TO SARS CoV-2 MAIN PROTEASE.....	30

SI TEXT 1: RDC SAMPLE PREPARATION

U-²H/¹³C/¹⁵N-enriched M^{pro}_{C145A} for RDC data acquisition was produced as described previously,¹⁻² with an additional refolding step to back-exchange buried amide protons. Briefly, this protocol involved expression of a GB1-M^{pro}_{C145A} fusion construct in the BL21(DE3) cells, in 99.8% ²H₂O, with ¹⁵N-NH₄Cl (Cambridge Isotopes) and U-²H,¹³C-Glucose (97-98% ²H, 99% ¹³C; Cambridge Isotopes) as the primary nitrogen and carbon sources (respectively), supplemented by 0.1 g/L ²H,¹³N,¹⁵N-Isogro (Isotec).

Isotropic (aligned) RDC spectra were acquired on a sample containing 0.6 mM (1.1 mM) ²H/¹³C/¹⁵N-M^{pro}_{C145A} in 10 mM sodium phosphate, pH 7.0, 0.5 mM TCEP, 3% v/v ²H₂O and 0.3 mM sodium trimethylsilylpropanesulfonate (DSS; as an internal chemical shift reference) in a 300-μL Shigemi microcell. ARTSY-HNCO (TATER) experiments to determine ¹D_{NH} (²D_{C,H}) RDCs were recorded at 35 °C on a 900 MHz (600 MHz) Bruker Neo spectrometer, equipped with a 5-mm TCI probe containing a z-axis gradient accessory, and running TopSpin software version 4.1. For aligned RDC measurements, Pfl phage stock solution (50 mg/mL, 10mM KPO₄, pH 7.6, 2mM MgCl₂, 0.05% NaN₃; AslaBiotech) was added to a final concentration of 11 mg/mL before being transferred to a 300 μL Shigemi microcell.

SI TEXT 2: ALPHAFOLD2 IMPLEMENTATION

The AlphaFold2 source code was retrieved from the official GitHub repository (<https://github.com/deepmind/alphafold>) and cloned (commit id: b1d772d127fcff4cc01d8fa1b4ea6e07da12193d) to a local computer. The requisite databases were retrieved with the included script. AlphaFold2 was run, unmodified, with a date limit of 01-01-3000 (full) or 01-01-2020 (date-limited) and otherwise default parameters.

For the sequence-limited calculation, the function “_assess_hsearch_hit” in file [repository base]/alphafold/data/templates.py was modified to measure the sequence similarity between each template sequence and the query sequence using an in-house implementation of the Smith-Waterman algorithm³ with BLOSUM62 weighting matrix⁴ and affine gap penalties (opening:12, extension:4).⁵ The distribution of alignment scores for the templates returned by hhsearch had a large gap between homologous sequences (containing all M^{pro}/3CL^{pro} sequences) and non-homologous sequences. A threshold value of 500 was chosen to exclude all homologous sequence.

Table S4 lists the templates used by AlphaFold2 in the three sets of model predictions.

The predicted AlphaFold2 models (with and without Amber relaxation), as well as the MSA results, modified AlphaFold2 python modules, and instructions for usage, can be downloaded from

<https://doi.org/10.5281/zenodo.5546136>

SI TEXT 3: RDC FITTING REGION BOUNDARY DETERMINATION

Analysis of >350 M^{pro} X-ray structures shows substantial heterogeneity at both the N- and C-termini, and in the loop-rich domain 2. Because RDCs are highly sensitive to small structural differences, we determined that fitting two contiguous regions in domains 1 and 3, avoiding the highly variable regions, would be most representative of the static structural differences across models. To determine the boundaries of these regions, we performed a search over the ranges 1-11 and 100-155 as boundaries for the domain 1 region, and 160-200 and 260-306 as boundaries for the domain 3 region. Initial boundary values were placed in the center of their allowed ranges. Regions were optimized using random search, whereby a random perturbation was made to the 4 boundary positions, each chosen from a discretized Cauchy distribution, and used to fit alignment tensors to all X-ray structures and AlphaFold models. Resulting Q factors for fits to all X-ray structures and AlphaFold models with given region definitions were averaged to a single value to act as a minimization target. A tabu list was kept to accelerate the search by avoiding repeat tests of the same boundary definitions. 1000 steps of random search were performed leading to a minimum Q factor of 0.254 with regions including residues 5-115 and 199-272. As expected, these boundaries reflect the increased spread in the X-ray structures near the N- and C-termini, and a larger spread in domain 2 and its linker to domain 3 (Fig. 2H). Analogously, the AF2 model also show higher ΔD values for these same regions.

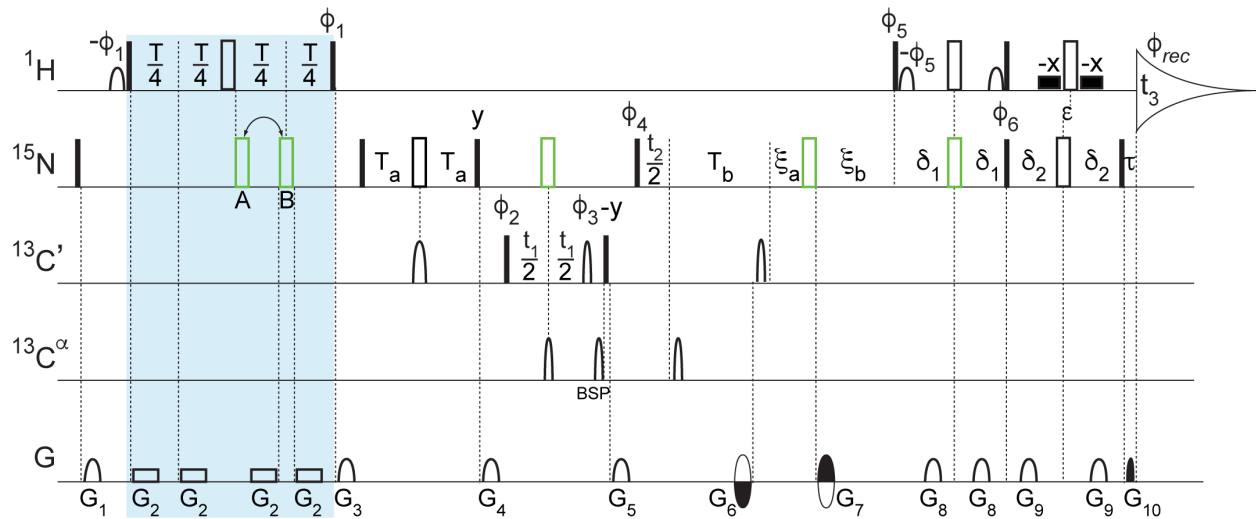


Figure S1: Pulse scheme of the ARTSY-HNCO experiment for measurement of ${}^1\text{D}_{\text{NH}}$ couplings in perdeuterated proteins. The pulse scheme is fully analogous to the standard TROSY-HNCO experiment,⁶ except that the initial INEPT transfer of ${}^1\text{H}$ to ${}^{15}\text{N}$ is lengthened to 10.75 ms $\approx 1/{}^1\text{J}_{\text{NH}}$, and a ${}^{15}\text{N}$ purge pulse prior to the first ${}^1\text{H}$ pulse followed by a gradient pulse (G_1) suppresses the ${}^{15}\text{N}$ Boltzmann magnetization for a 2-scan experiment. For a 4-scan experiment, $\pm y$ ${}^1\text{H}$ phase cycling of the $90^\circ \phi_1$ pulse is used to eliminate the ${}^{15}\text{N}$ Boltzmann magnetization. The experiment is executed twice, in an interleaved manner, with the position of the first ${}^{15}\text{N}$ 180° pulse alternately applied (A) immediately after the ${}^1\text{H}$ 180° pulse, corresponding to 10.75 ms ${}^1\text{J}_{\text{NH}} + {}^1\text{D}_{\text{NH}}$ dephasing, and (B) at the midpoint between the ${}^1\text{H}$ 180° pulse and the $90^\circ \phi_1$ pulse, corresponding to 5.38 ms ${}^1\text{J}_{\text{NH}} + {}^1\text{D}_{\text{NH}}$ dephasing. The intensity ratio of signals observed in the two spectra provides a direct measure for ${}^1\text{J}_{\text{NH}} + {}^1\text{D}_{\text{NH}}$.⁷ The data was recorded with the NUS setup but 100% sampling on a 900 MHz Bruker NEO spectrometer equipped with a 5-mm TCI probe containing a z-axis gradient accessory, and running Topspin software version 4.1.0. Filled and open rectangular bars on the ${}^1\text{H}$ and ${}^{15}\text{N}$ channels represent 90° and 180° pulses, respectively. Open bars in green represent composite 180° ${}^{15}\text{N}$ pulses consisting of $90^\circ_x 220^\circ_y 90^\circ_x$. The open ${}^1\text{H}$ shaped pulses represent 90° water-flipback pulses (center lobe of a sinc profile, 1.9-ms duration at 900 MHz)⁸. The wide filled rectangular boxes denote 90° water-flipback pulses (1.0-ms duration at 900 MHz). The open shaped pulses in the ${}^{13}\text{C}'$ channel represent sinc pulses (centered at 176 ppm; 100 μs duration at 226.37 MHz ${}^{13}\text{C}$ frequency) for ${}^{13}\text{C}'$ inversion, while the open shaped ${}^{13}\text{C}^\alpha$ pulses are Q3 decoupling pulses⁹ (200 μs at 226.37 MHz ${}^{13}\text{C}$ frequency). The segment shaded in blue highlights the ARTSY scheme to obtain the reference and attenuated spectra. Unless indicated otherwise, all pulses are applied along x. The following delays were used: $T = 10.92$ ms (slightly longer than the effective coupling evolution time of 10.75 ms in the attenuated experiment to accommodate the composite ${}^{15}\text{N}$ 180° pulse), $\delta_1 = 2.35$ ms, $\delta_2 = 2.7$ ms, $T_a = 12$ ms, $T_b = 12.5$ ms, $\xi_a = \max(0, t_1/2 - T_b)$, $\xi_b = \max(0, T_b - t_1/2)$. The ${}^1\text{H}$ chemical shift evolution during the gradient decoding delay $\tau = 0.3$ ms was compensated by offsetting the last pair of ${}^1\text{H}$ and ${}^{15}\text{N}$ 180° pulses by $\varepsilon = \tau/2$ to avoid the linear phase error in the t_3 dimension. Phase cycling: $\phi_1 = y, y, -y, -y$, $\phi_2 = y, \phi_3 = x, y, -x, -y$, $\phi_4 = y, \phi_5 = -y, \phi_6 = -y$, $\phi_{\text{rec}} = x, -x, -x, x$; gradients were sine-bell or rectangular shaped (as depicted in the figure) with durations $G_{1,2,3,4,5,6,7,8,9,10} = 1.0, 2.53, 1.1, 0.5, 0.5, 0.5, 0.5, 0.24, 1.1$, and 0.101 ms, and z-strengths of 16.1, 0.14, 1.4, 3.5, 28, 38.5, -31.5, 0.35, 32.9, and 35 G/cm, respectively. The duration of decoding pulses G_{10} was empirically optimized for maximum signal and can differ from the theoretical value derived from the gyromagnetic ratios of ${}^{15}\text{N}$ and ${}^1\text{H}$ and the encoding pulses G_6+G_7 by several microseconds due to rise and fall times of short gradient pulses. Quadrature detection in t_2 was achieved using the Echo-AntiEcho scheme¹⁰ by inverting the encoding gradient G_6 and G_7 together with ϕ_5 and ϕ_6 to obtain the second FID for every t_2 increment. The t_1 dimension was acquired using States-TPPI by incrementing ϕ_2 by 90° . The Bruker pulse program and parameter files can be downloaded from <https://doi.org/10.5281/zenodo.5546136>.

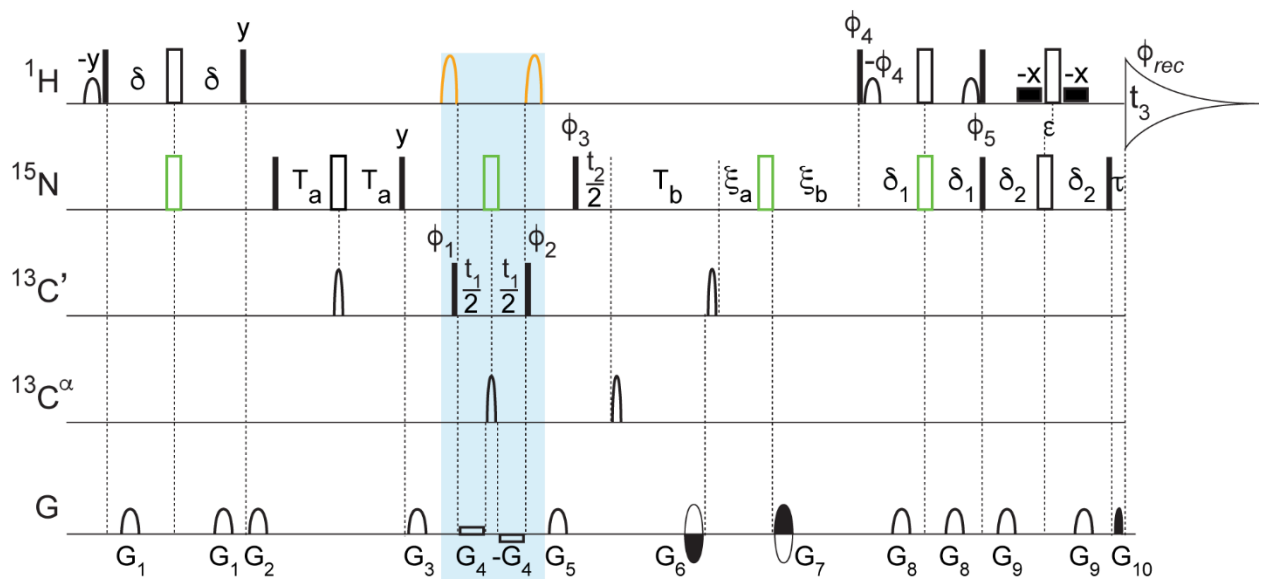


Figure S2: Pulse scheme of the TATER experiment for measurement of two-bond $^{13}\text{C}'\text{-H}^{\text{N}}$ RDCs in perdeuterated proteins. Two interleaved spectra are recorded: (1) a regular TROSY-HNCO spectrum,⁶ and (2) a spectrum where all protons are inverted by tanh/tan adiabatic ^1H 180° pulses immediately preceding and following the $^{13}\text{C}'$ evolution period. The difference in $^{13}\text{C}'$ resonance frequencies corresponds to the sum of $^2\text{J}_{\text{C}'\text{HN}}$ and $^2\text{D}_{\text{C}'\text{HN}}$. The experiment yields highest precision when $^{13}\text{C}'$ acquisition extends to *ca* $1.5 \times T_2(^{13}\text{C}')$. The data for the isotropic sample was recorded with 74.8% non-uniform sampling, while 100% NUS was applied for the aligned sample. The filled and open rectangular bars on the ^1H and ^{15}N channels represent 90° and 180° pulses, respectively. The open bars in green represent composite 180° ^{15}N pulses consisting of 90° \times 220° \times 90° \times . Open ^1H shaped pulses represent 90° water-flipback pulses (center lobe of a sinc profile; 1.9-ms duration at 600 MHz).⁸ Open shaped pulses in orange are adiabatic tanh/tan ^1H inversion pulses (1.0-ms duration with the frequency sweeping width of 1 MHz at 600 MHz) and are applied only in the antiTROSY experiment.¹¹ The segment shaded in blue highlights the segment for the coupling measurement. Wide, filled rectangular boxes denote rectangular 90° water-flipback pulses (1.0-ms duration at 600 MHz). Open shaped $^{13}\text{C}'$ pulses represent sinc pulses (150 μs at 150.9 MHz ^{13}C frequency) for $^{13}\text{C}'$ inversion, while the open shaped pulses in the $^{13}\text{C}^{\alpha}$ channel are Q3 decoupling pulses⁹ (200 μs at 150.9 MHz ^{13}C frequency). Unless indicated otherwise, all pulses were applied along x. The following delays were used: $\delta = 2.35$ ms, $\delta_1 = 2.35$ ms, $\delta_2 = 2.7$ ms. $T_a = 12$ ms, $T_b = 12.5$ ms, $\xi_a = \max(0, t_1/2 - T_b)$, $\xi_b = \max(0, T_b - t_1/2)$. The ^1H chemical shift evolution during the delay $\tau = 0.3$ ms was compensated by offsetting the last pair of ^1H and ^{15}N 180° pulses by $\varepsilon = \tau/2$ to avoid a linear phase error in the t_3 dimension. Phase cycling: $\phi_1 = y$, $\phi_2 = y, -y$, $\phi_3 = y, y, -x, -x$, $\phi_4 = -y$, $\phi_5 = -y$, $\phi_{\text{rec}} = y, -y, x, -x$; gradients were sine-bell or rectangular shaped (as depicted in the figure) with durations $G_{1,2,3,4,5,6,7,8,9,10} = 1.8, 0.5, 0.5, 0.5, 0.5, 0.24, 0.7$ and 0.1013 ms, z-strengths of 7.7, 4.2, 25.9, 1.19, 28.7, 37.1, -30.1, 6.3, 37.1, and 33.6 G/cm, respectively. The duration of decoding pulses G_{10} was empirically optimized for maximum signal and can differ from the theoretical value derived from the gyromagnetic ratios of ^{15}N and ^1H and the encoding pulses $G_6 + G_7$ by several microseconds due to rise and fall times of short gradient pulses. Quadrature detection in t_2 was achieved using the Echo-AntiEcho scheme¹⁰ by inverting the encoding gradient G_6 and G_7 together with ϕ_5 and ϕ_6 and changing ϕ_3 to y, y, x, x to obtain the second FID for every t_2 increment. The t_1 dimension was acquired using States-TPPI by incrementing ϕ_2 by 90°. Because $T_2(^{13}\text{C}')$ is dominated by chemical shift anisotropy, the experiment is best recorded at medium magnetic field strengths, i.e., 500 or 600 MHz ^1H frequency. The Bruker pulse program and parameter files can be downloaded from <https://doi.org/10.5281/zenodo.5546136>

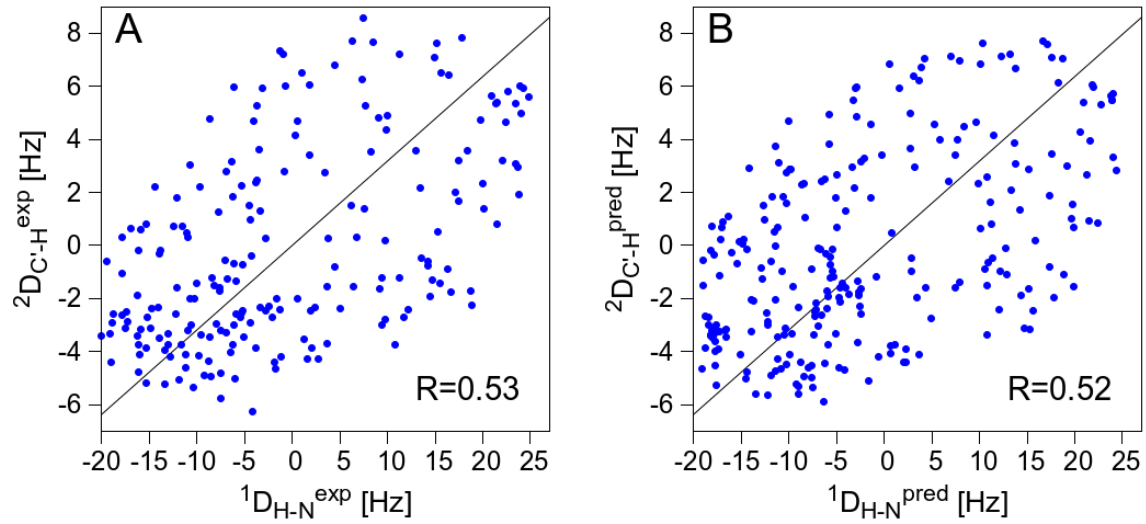


Figure S3: Correlation between $^1\text{D}_{\text{NH}}$ and $^2\text{D}_{\text{C}-\text{H}}$ couplings in M^{pro}. (A) For 204 experimentally observed pairs of couplings where the estimated uncertainty in $^1\text{D}_{\text{NH}}$ is $\leq 2\text{Hz}$ and the $^2\text{D}_{\text{C}-\text{H}}$ uncertainty is $\leq 0.7 \text{ Hz}$. (B) For RDC values predicted for PDB entry 5R8T, using the best-fitted alignment tensor obtained from the experimental data. All backbone amides are included. The high degree of scatter between $^1\text{D}_{\text{NH}}$ and $^2\text{D}_{\text{C}-\text{H}}$ (Pearson's correlation coefficient $R^2 \approx 0.285$ (A) and 0.280 (B)) indicates the measurements are reasonably independent of one another.

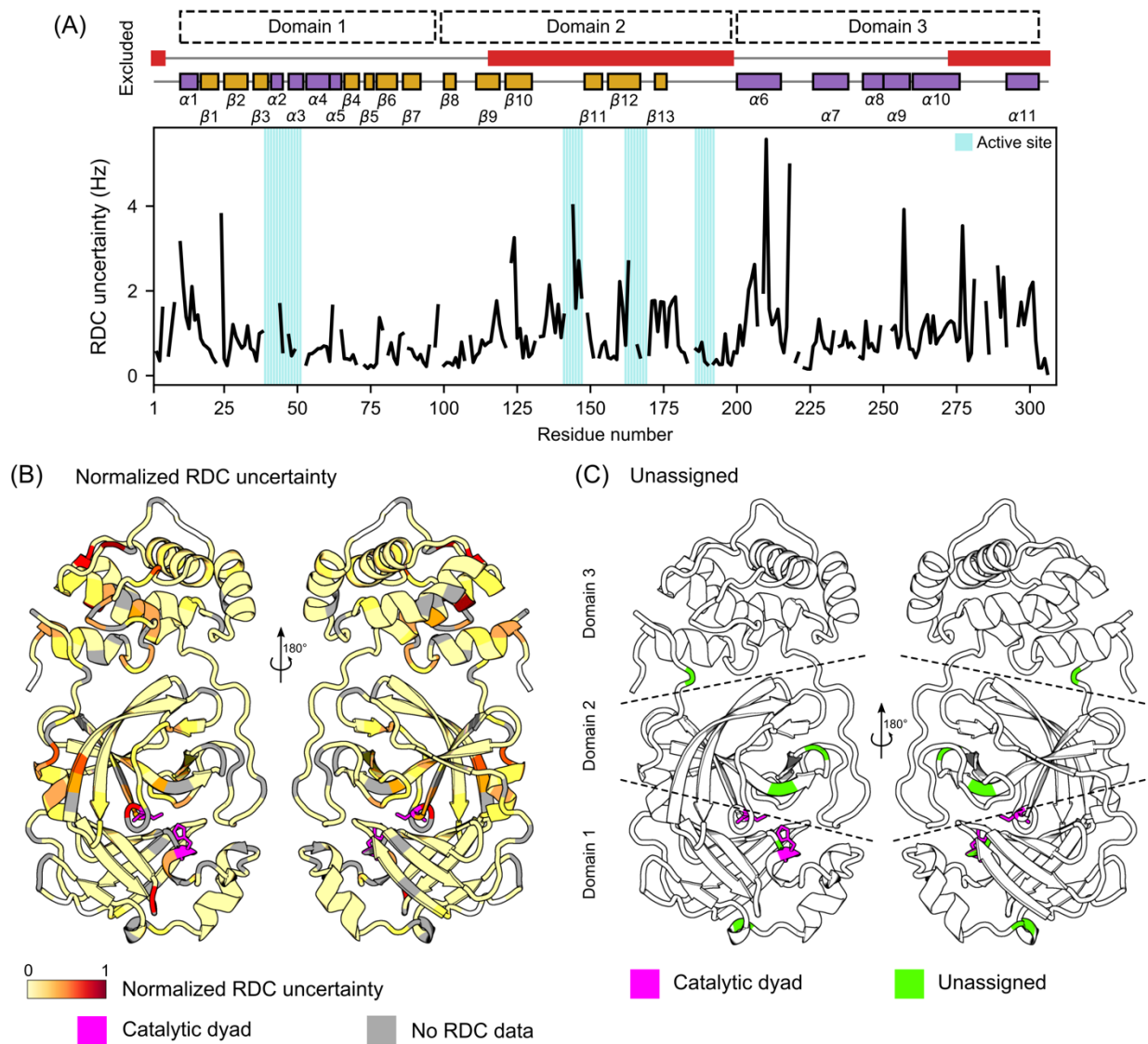


Figure S4: Magnitude of experimental RDC uncertainties for the ARTSY-HNCO and TATER experiments. (A) RDC uncertainty by residue, where the overall RDC uncertainty $\sigma_T = (\sigma_{\text{NH}} + \alpha\sigma_{\text{C}\text{H}}) / 2$, is determined with a scaling factor $\alpha=3.238$ to account for differences in dipolar interaction strength. Secondary structure annotations (α -helix: purple; β -sheet: yellow) were obtained from the header of PDB 5R8T, with domain partitioning and excluded regions (red) also indicated. The uncertainty scales inversely with the signal-to-noise ratio of the corresponding HNCO resonance, and indirectly reflects conformational exchange broadening and/or hydrogen exchange with solvent. (B) The RDC uncertainties were normalized relative to the largest uncertainty (residue 210) and plotted on PDB 5R8T as a color-ramp, from white to red. Residues without usable RDC data were colored grey. These missing RDCs were either due to low peak intensity (indicating either dynamics, or hydrogen exchange), or due to missing assignments. (C) Illustrates residues with missing assignments in $\text{M}^{\text{pro}}_{\text{C}145\text{A}}$ (green), with the catalytic dyad for M^{pro} colored purple in both (B) and (C).

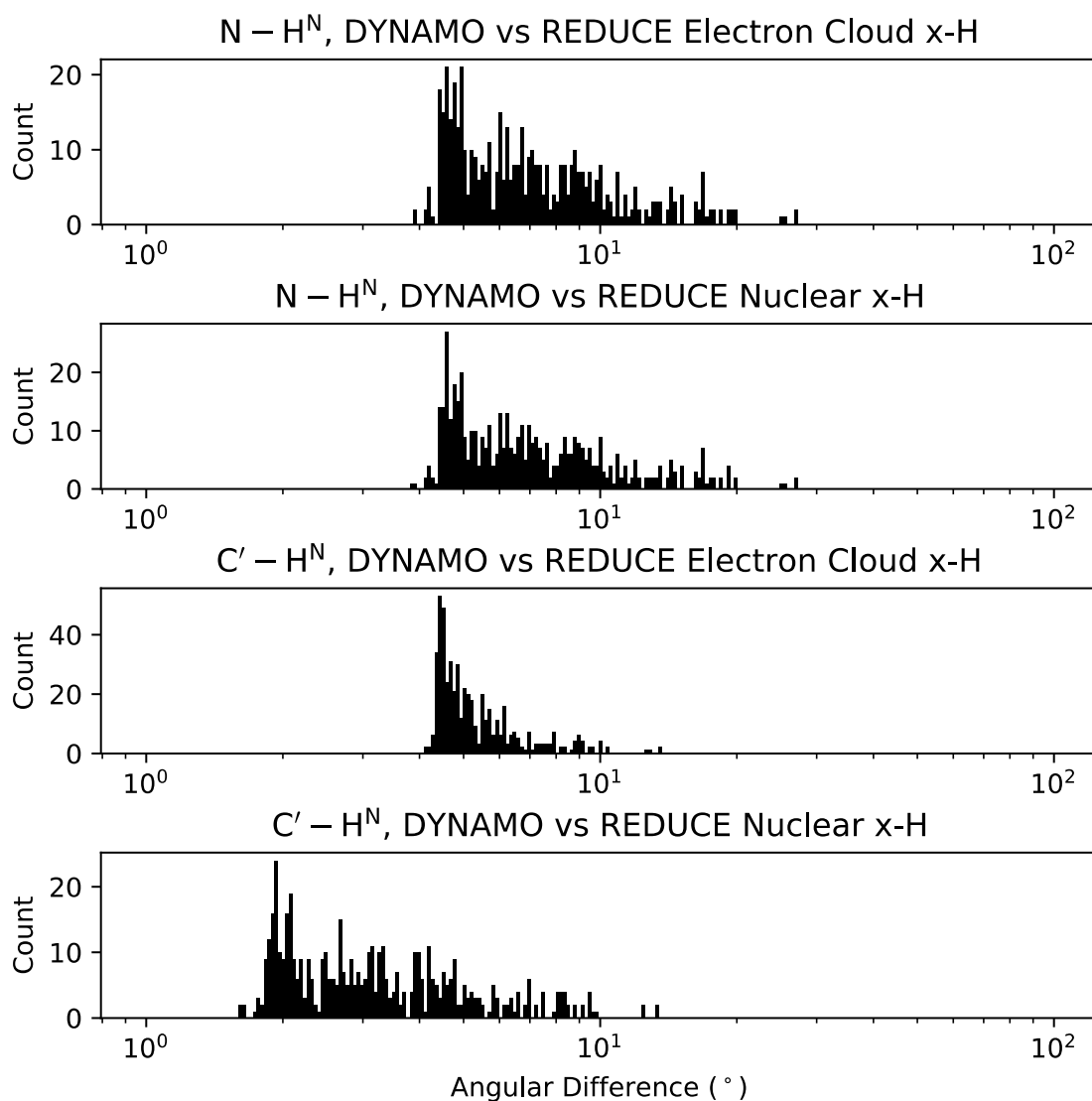


Figure S5: Protonation method dependence of N-H^N and C'-H^N vector orientation. The X-ray structure PDB 5R8T (where residues with alternate locations were separated into Chain A and Chain B) was protonated using three different methods; DYNAMO (NMRPipe¹² software suite), REDUCE¹³ (Electron Cloud x-H), and REDUCE (Nuclear x-H), and a pairwise comparison of N-HN and C'-HN vectors was made as indicated in the figure titles. For predicting ²D_CH couplings, all N-H bond lengths were scaled to 0.99 Å. An SVD fit of the protonated structures to the RDC data give Q-factors; DYNAMO 0.284 (0.208/0.356), REDUCE Electron Cloud 0.336 (0.284/0.387), REDUCE Nuclear x-H 0.320 (0.263/0.381), for all residues (included region/excluded region).

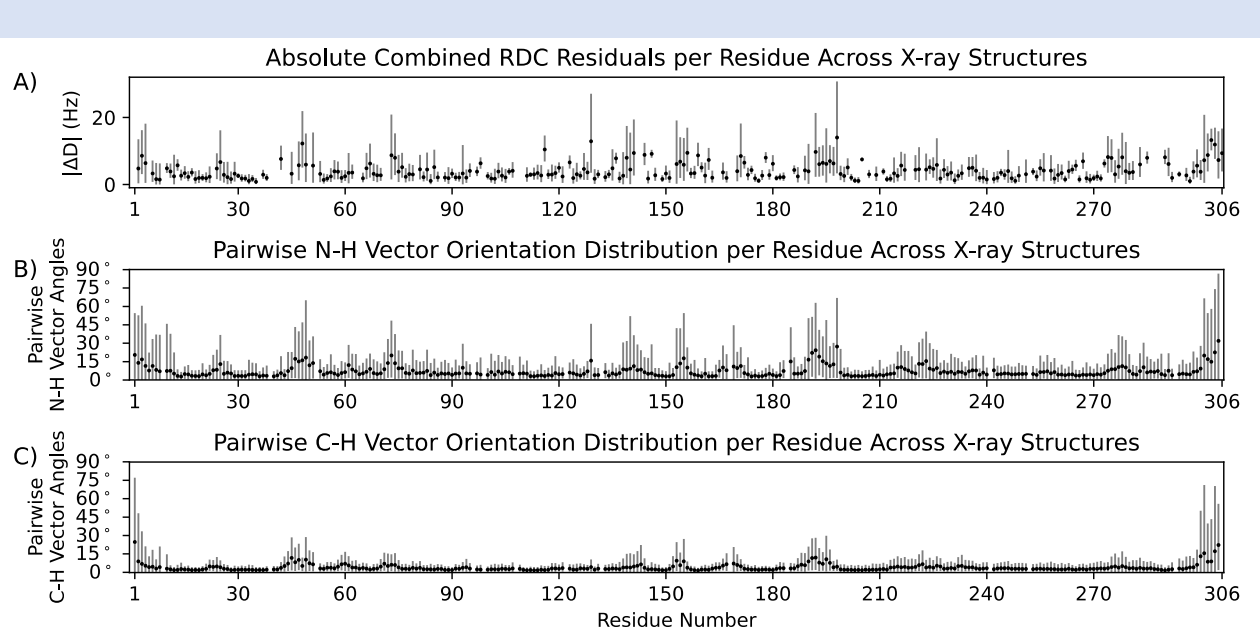


Figure S6: Distribution of RDC residuals and dipolar interaction vector orientations across X-ray structures. (A) Average (dots) and 5-95% ranges (vertical lines) for the absolute combined RDC residual ($|\Delta D|$) for each residue, across X-ray structures of M^{pro} . The large average and wide range of disagreement with experimental RDCs in the termini and central domain 2 are evident. (B-C) Average (dots) and 5-95% ranges (vertical lines) of pairwise angles between (B) N-H and (C) C-H dipolar interaction vectors, per residue, across X-ray structures of M^{pro} . High variability in the termini and central domain 2 are reflected in the wide distributions of N-H and C-H^N vector orientations.

Figure S7: Effect of Amber relaxation on predicted RDCs. RDCs are predicted for the Amber-relaxed (y-axis) and unrelaxed (x-axis) models, generated by the full AlphaFold2 implementation (termed M^{pro}_{AF} in the main text – see implementation details below). The left column of figures is for $^1D_{NH}$ couplings; the right column is for $^2D_{CH}$ couplings.

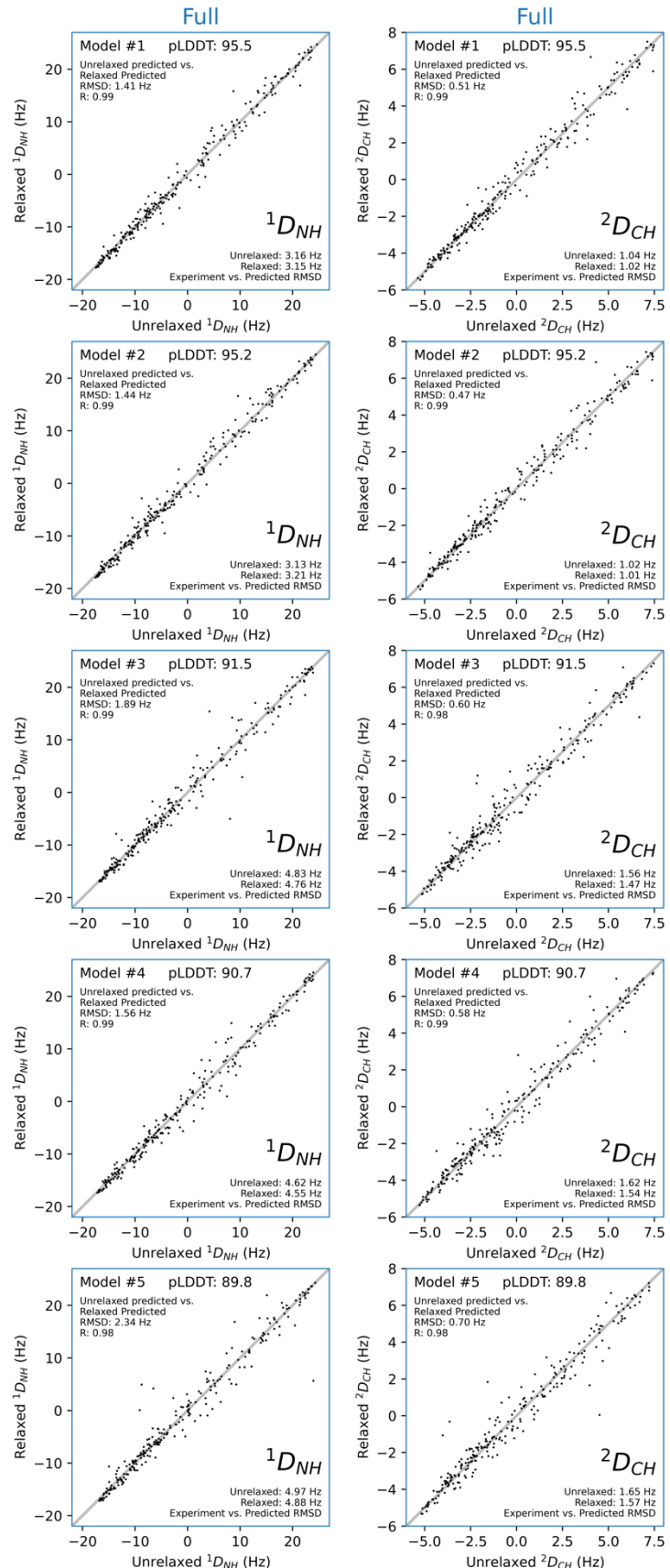


Figure S8: Effect of Amber relaxation on predicted RDCs. RDCs are predicted for the Amber-relaxed (y-axis) and unrelaxed (x-axis) models, generated by date-restricted AlphaFold2 implementation (termed M^{pro}_{AFD} in the main text – see implementation details below). The left column of figures is for ¹D_{NH} couplings; the right column is for ²D_{C'H} couplings.

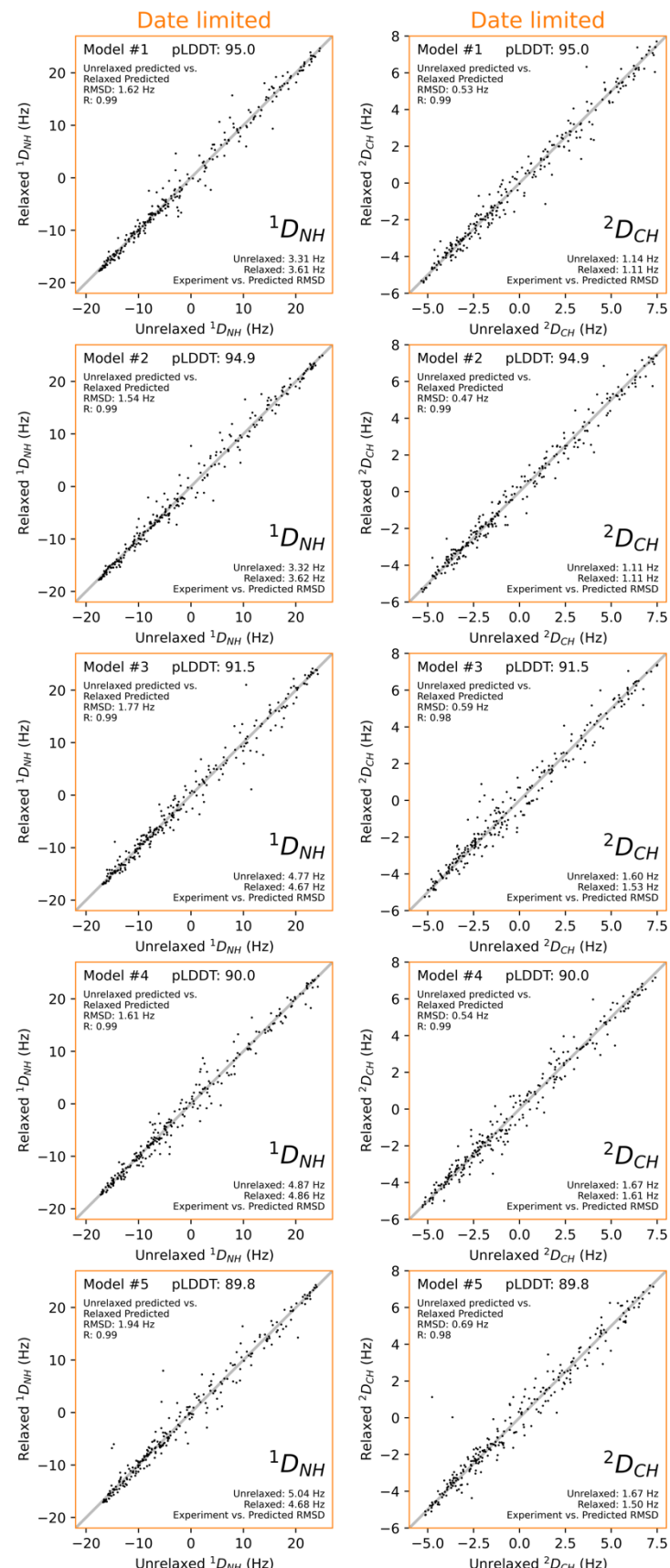
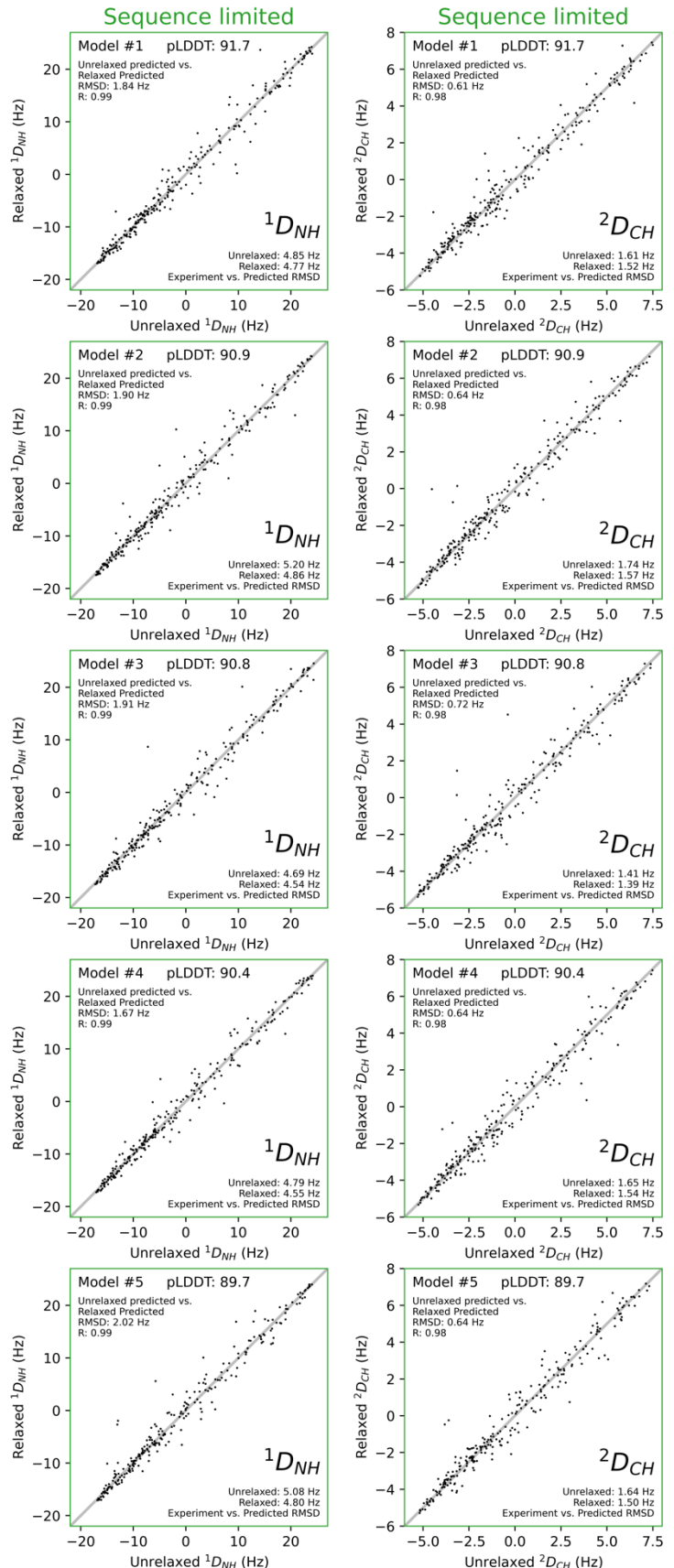


Figure S9: Effect of Amber relaxation on predicted RDCs. RDCs are predicted for the Amber-relaxed (y-axis) and unrelaxed (x-axis) models, generated by the sequence-restricted AlphaFold2 implementation (termed M^{PRO}_{AFS} in the main text – see implementation details below). The left column of figures is for ¹D_{NH} couplings; the right column is for ²D_{CH} couplings.



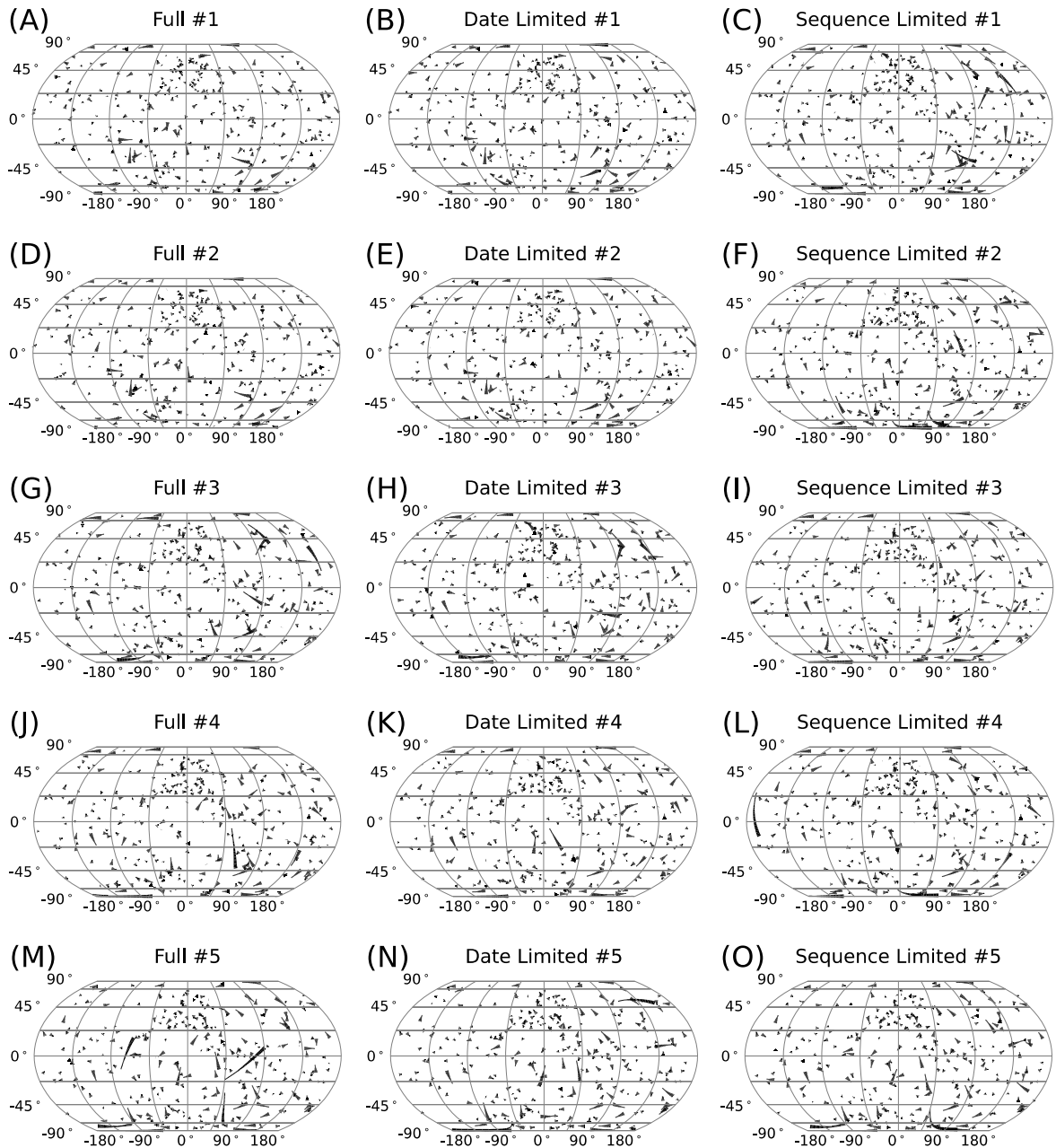


Figure S10: Effect of Amber relaxation on N-H bond vector orientations of the AlphaFold2 models. All AlphaFold2-predicted structures were aligned by alpha carbons to PDB 5R8T, and the changes in N-H bond vector orientations are shown as comets moving from unrelaxed (narrow comet tail) to relaxed (wide comet body) orientations. Full calculation results ranked by average pLDDT are shown in the left column (A, D, G, J, M). Date-limited results are shown in the center column (B, E, H, K, N). Sequence-limited results are shown in the right column (C, F, I, L, O).

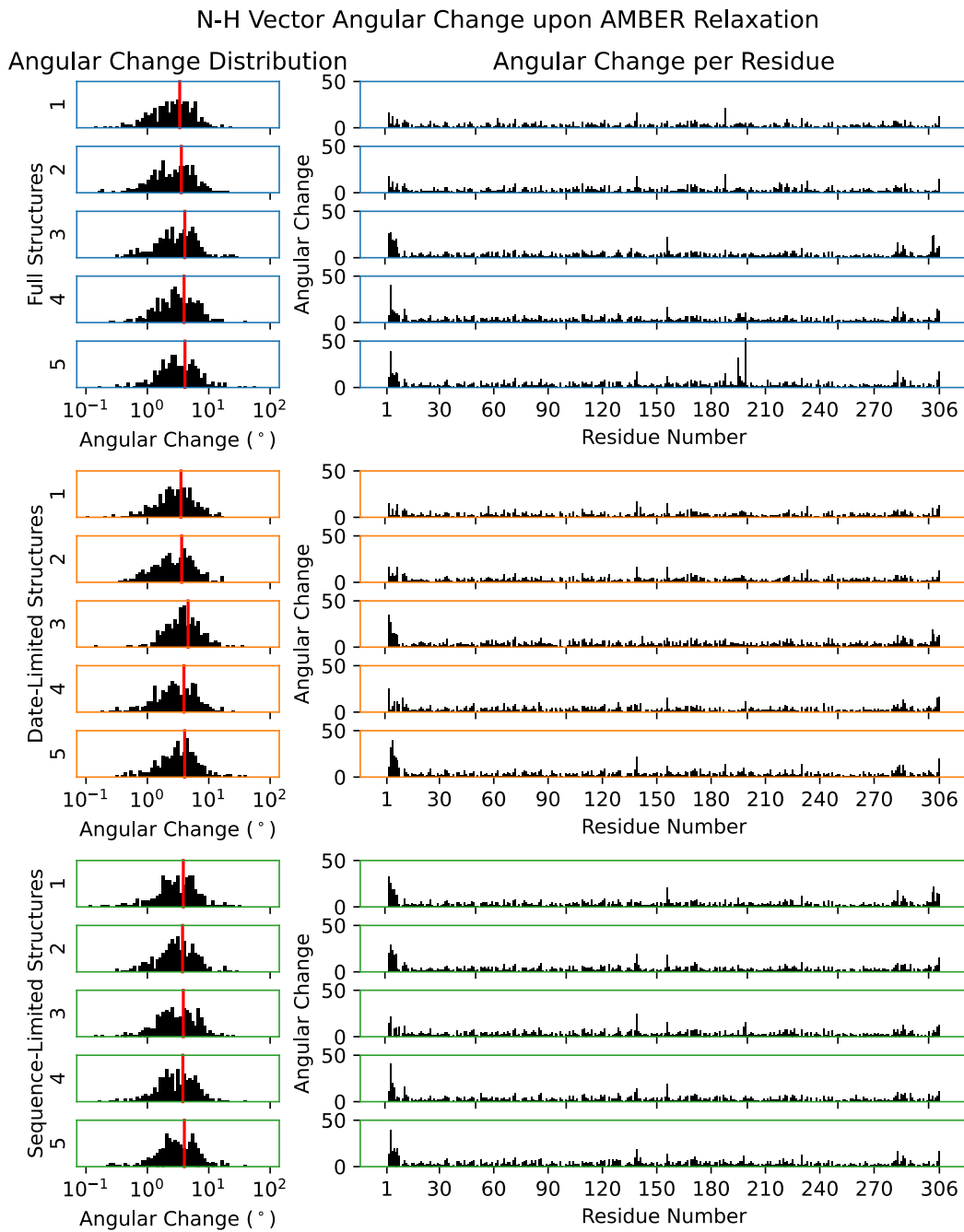


Figure S11: Magnitude of N-H bond vector orientational change upon Amber relaxation of the AlphaFold2 models. (Left Column) Histograms of the distribution of absolute angular changes between N-H vectors in unrelaxed and relaxed AlphaFold models, with the abscissa plotted on a log scale Average change is indicated by red vertical lines. Typical changes were *ca* 4° but much larger changes were observed for multiple residues. (Right Column) Magnitude of angular change per residue across Alphafold2 models. Angular changes were primarily concentrated in the termini with several large rearrangements in loop-rich domain 2.

Table S1: Acquisition, NUS sampling, and SMILE reconstruction parameters for the TATER and ARTSY-HNCO experiments.

Experiment	ARTSY-HNCO			TATER		
Dimension	F ₃	F ₂	F ₁	F ₃	F ₂	F ₁
Nucleus observed	¹ H	¹⁵ N	¹³ C	¹ H	¹⁵ N	¹³ C
Quadrature detection	Dire ct	Ech o-AntiEcho	Sta tes-TPPI	Dir ect	Ech o-AntiEcho	Stat es-TPPI
Topspin TD size	3072	320	52	204 8	260	110
No. of increment (i.e. complex pairs)	1536	160	26	102 4	130	55
Extended No. of increment by SMILE	n/a	n/a	n/a	n/a	195	82
Spectral width (Hz)	1315 7.9	2907 .7	322 5.8	862 0.7	200 0.0	181 8.2
Acquisition time (msec)	116. 7	55.0	8.1	118 .8	65. 0	30. 3
SMILE extended acquisition time (msec)	n/a	n/a	n/a	118 .8	97. 5	45. 1
Topspin NUS T ₂ for exp. weighting (sec)	n/a	n/a	n/a	n/a	1.0	1.0
Topspin NUS sampling random seed	n/a			n/a	54321	
NUS sampling percentage (effective)	n/a			n/a	74.8% (33.4%) ^a	
Total No. of FID recorded	33280			42776		
No of real points in the spectrum	1598	1024	128	814	102 4	512
Spectrum digital resolution (Hz/point)	3.21	2.84	25. 20	4.2 1	1.9 5	3.5 5
No. of threads for SMILE ^b	n/a			32		
Max allowed memory for SMILE (GB)	n/a			402.8 (6.7) ^c		
SMILE reconstruction time (min) ^d	n/a			1.05		

^a Effective sampling percentage after the default 50% SMILE extension in each of the indirect dimensions

^b Reconstruction running on a Ubuntu 20.0 workstation with 32 Intel Xeon Gold 6226R CPUs (2.90 GHz) and 512 GB memory available

^c Actual amount of memory allocated by SMILE

^d Wall time for the SMILE reconstruction of both HNCO spectra, not including the data conversion, expansion, and post-reconstruction conventional NMRPipe processing time

Table S2: Table of experimental couplings (Hz) and their associated error (Hz) derived from the ARTSY-HNCO (254/292 non-Pro) and TATER (257/292 non-Pro) experiments. Columns for ARTSY-HNCO (TATER) correspond to: Isotropic $^1\text{J}_{\text{NH}}$ ($^2\text{J}_{\text{C}'\text{H}}$), Aligned $^1\text{J}_{\text{NH}} + ^1\text{D}_{\text{NH}}$ ($^2\text{J}_{\text{C}'\text{H}} + ^2\text{D}_{\text{C}'\text{H}}$), and RDC $^1\text{D}_{\text{NH}}$ ($^2\text{D}_{\text{C}'\text{H}}$) couplings. Experimental errors were propagated as fractional errors using either 30/SN (ARTSY-HNCO) or an empirically determined LW / (0.6*SN) (TATER) peak position uncertainty, where SN denotes the signal-to-noise ratio of the resonance. The solvent ^2H quadrupolar splitting was 12.8 Hz for the ARTSY-HNCO experiment, and 11.5 Hz for the TATER experiment.

Residue	ARTSY-HNCO			TATER		
	Isotropic	Aligned	RDC	Isotropic	Aligned	RDC
S1	-	-	-	-	-	-
G2	91.4 \pm 0.2	100.4 \pm 0.2	9.0 \pm 0.2	4.7 \pm 0.2	9.0 \pm 0.1	4.3 \pm 0.3
F3	91.3 \pm 0.1	95.8 \pm 0.1	4.4 \pm 0.2	4.6 \pm 0.1	3.9 \pm 0.1	-0.7 \pm 0.2
R4	94.5 \pm 0.8	102.9 \pm 0.8	8.4 \pm 1.1	3.7 \pm 0.5	10.5 \pm 0.4	6.8 \pm 0.6
K5	-	-	-	-	-	-
M6	92.3 \pm 0.2	91.0 \pm 0.2	-1.3 \pm 0.3	3.9 \pm 0.2	1.7 \pm 0.1	-2.2 \pm 0.2
A7	89.8 \pm 0.5	78.9 \pm 0.5	-10.9 \pm 0.7	4.7 \pm 0.4	5.0 \pm 0.3	0.3 \pm 0.5
F8	92.8 \pm 0.7	77.5 \pm 0.8	-15.2 \pm 1.1	3.6 \pm 0.5	-0.2 \pm 0.5	-3.8 \pm 0.7
P9	-	-	-	-	-	-
S10	92.9 \pm 1.3	86.9 \pm 1.3	-6.0 \pm 1.9	4.2 \pm 0.8	0.9 \pm 1.1	-3.3 \pm 1.4
G11	95.0 \pm 1.0	84.3 \pm 1.1	-10.7 \pm 1.5	5.6 \pm 0.6	2.0 \pm 0.7	-3.6 \pm 0.9
K12	94.0 \pm 0.5	96.7 \pm 0.5	2.7 \pm 0.7	5.4 \pm 0.5	4.5 \pm 0.4	-0.9 \pm 0.6
V13	92.5 \pm 0.4	89.4 \pm 0.4	-3.1 \pm 0.5	4.8 \pm 0.4	10.1 \pm 0.4	5.3 \pm 0.5
E14	92.7 \pm 0.9	83.1 \pm 1.0	-9.6 \pm 1.3	4.2 \pm 0.6	0.3 \pm 0.7	-4.0 \pm 0.9
G15	94.6 \pm 0.4	85.0 \pm 0.4	-9.6 \pm 0.6	5.6 \pm 0.4	2.6 \pm 0.4	-3.0 \pm 0.6
C16	91.1 \pm 0.6	106.1 \pm 0.6	15.0 \pm 0.9	4.7 \pm 0.4	11.1 \pm 0.5	6.4 \pm 0.6
M17	94.2 \pm 0.3	74.2 \pm 0.3	-20.0 \pm 0.4	4.3 \pm 0.3	1.2 \pm 0.3	-3.1 \pm 0.4
V18	92.5 \pm 0.2	96.2 \pm 0.2	3.7 \pm 0.3	4.5 \pm 0.3	1.1 \pm 0.2	-3.3 \pm 0.4
Q19	92.3 \pm 0.2	114.4 \pm 0.3	22.0 \pm 0.4	4.2 \pm 0.2	7.0 \pm 0.2	2.9 \pm 0.3
V20	93.0 \pm 0.2	117.9 \pm 0.3	24.8 \pm 0.4	4.9 \pm 0.2	9.9 \pm 0.2	5.0 \pm 0.3
T21	92.6 \pm 0.1	116.9 \pm 0.2	24.2 \pm 0.2	5.3 \pm 0.1	10.6 \pm 0.1	5.3 \pm 0.2
C22	93.5 \pm 0.1	114.4 \pm 0.1	20.9 \pm 0.2	5.1 \pm 0.1	10.1 \pm 0.1	5.0 \pm 0.1
G23	-	-	-	-	-	-
T24	91.3 \pm 1.0	81.8 \pm 1.1	-9.5 \pm 1.5	5.2 \pm 1.8	9.9 \pm 0.7	4.8 \pm 1.9
T25	92.9 \pm 0.1	96.5 \pm 0.1	3.7 \pm 0.2	4.5 \pm 0.1	3.1 \pm 0.1	-1.4 \pm 0.2
T26	91.9 \pm 0.1	109.3 \pm 0.1	17.5 \pm 0.1	4.5 \pm 0.1	6.0 \pm 0.1	1.5 \pm 0.1
L27	93.4 \pm 0.3	117.1 \pm 0.4	23.7 \pm 0.4	4.0 \pm 0.2	6.7 \pm 0.2	2.7 \pm 0.2
N28	92.1 \pm 0.6	115.6 \pm 0.8	23.5 \pm 1.0	4.6 \pm 0.3	7.4 \pm 0.3	2.8 \pm 0.4
G29	91.9 \pm 0.3	85.6 \pm 0.3	-6.3 \pm 0.5	4.5 \pm 0.3	7.3 \pm 0.3	2.8 \pm 0.4
L30	91.5 \pm 0.3	75.5 \pm 0.3	-16.0 \pm 0.5	4.1 \pm 0.3	0.5 \pm 0.2	-3.7 \pm 0.3
W31	88.9 \pm 0.3	77.7 \pm 0.3	-11.2 \pm 0.4	5.3 \pm 0.2	1.7 \pm 0.2	-3.7 \pm 0.3

L32	94.2 ± 0.2	75.3 ± 0.3	-19.0 ± 0.4	4.6 ± 0.2	0.7 ± 0.2	-4.0 ± 0.3
D33	95.4 ± 0.4	78.1 ± 0.5	-17.3 ± 0.7	5.4 ± 0.4	2.9 ± 0.3	-2.6 ± 0.5
D34	92.8 ± 0.2	85.9 ± 0.2	-6.9 ± 0.3	5.3 ± 0.2	2.3 ± 0.2	-2.9 ± 0.3
V35	94.1 ± 0.2	79.7 ± 0.2	-14.4 ± 0.3	5.4 ± 0.2	7.3 ± 0.2	2.0 ± 0.3
V36	92.6 ± 0.2	80.8 ± 0.3	-11.8 ± 0.3	-	-	-
Y37	94.0 ± 0.4	74.6 ± 0.5	-19.4 ± 0.6	3.9 ± 0.3	3.3 ± 0.3	-0.5 ± 0.4
C38	94.4 ± 0.4	82.6 ± 0.5	-11.8 ± 0.7	5.4 ± 0.3	0.9 ± 0.3	-4.5 ± 0.4
P39	-	-	-	-	-	-
R40	-	-	-	-	-	-
H41	-	-	-	-	-	-
V42	94.1 ± 0.6	84.5 ± 0.6	-9.6 ± 0.9	4.6 ± 1.0	4.3 ± 0.6	-0.3 ± 1.2
I43	-	-	-	-	-	-
C44	-	-	-	4.3 ± 0.4	6.7 ± 0.3	2.3 ± 0.5
T45	90.8 ± 0.2	75.5 ± 0.3	-15.3 ± 0.3	4.3 ± 0.2	-0.3 ± 0.2	-4.7 ± 0.2
S46	-	-	-	-	-	-
E47	92.4 ± 0.2	105.8 ± 0.3	13.4 ± 0.3	5.0 ± 0.4	6.9 ± 0.3	2.0 ± 0.5
D48	92.3 ± 0.1	91.6 ± 0.1	-0.8 ± 0.2	4.8 ± 0.2	7.3 ± 0.1	2.5 ± 0.2
M49	91.8 ± 0.3	86.4 ± 0.3	-5.4 ± 0.4	4.2 ± 0.2	1.8 ± 0.2	-2.4 ± 0.3
L50	-	-	-	-	-	-
N51	93.0 ± 0.1	100.4 ± 0.1	7.4 ± 0.2	4.5 ± 0.2	10.1 ± 0.1	5.6 ± 0.2
P52	-	-	-	-	-	-
N53	93.0 ± 0.1	89.2 ± 0.1	-3.8 ± 0.1	4.8 ± 0.1	6.9 ± 0.1	2.1 ± 0.1
Y54	93.4 ± 0.2	107.9 ± 0.2	14.5 ± 0.3	4.6 ± 0.2	2.9 ± 0.2	-1.7 ± 0.2
E55	92.9 ± 0.2	109.5 ± 0.2	16.6 ± 0.3	5.1 ± 0.2	3.6 ± 0.2	-1.6 ± 0.2
D56	93.0 ± 0.2	117.0 ± 0.2	24.0 ± 0.3	5.0 ± 0.2	9.4 ± 0.2	4.4 ± 0.3
L57	93.9 ± 0.2	111.3 ± 0.3	17.5 ± 0.3	4.6 ± 0.2	7.5 ± 0.2	2.9 ± 0.3
L58	93.6 ± 0.2	104.9 ± 0.2	11.2 ± 0.3	4.8 ± 0.2	3.7 ± 0.2	-1.1 ± 0.3
I59	92.1 ± 0.3	110.8 ± 0.3	18.8 ± 0.4	4.1 ± 0.2	2.6 ± 0.2	-1.5 ± 0.3
R60	93.0 ± 0.2	114.3 ± 0.3	21.4 ± 0.4	4.4 ± 0.2	9.2 ± 0.2	4.8 ± 0.3
K61	93.1 ± 0.1	91.4 ± 0.1	-1.7 ± 0.1	4.5 ± 0.1	2.7 ± 0.1	-1.8 ± 0.2
S62	95.5 ± 0.8	87.5 ± 0.8	-8.0 ± 1.1	4.3 ± 0.6	1.7 ± 0.3	-2.5 ± 0.7
N63	-	-	-	-	-	-
H64	-	-	-	-	-	-
N65	91.6 ± 0.4	83.1 ± 0.4	-8.4 ± 0.6	4.7 ± 0.3	3.6 ± 0.3	-1.1 ± 0.5
F66	92.2 ± 0.1	109.4 ± 0.2	17.2 ± 0.2	4.6 ± 0.1	6.4 ± 0.1	1.8 ± 0.2
L67	92.7 ± 0.1	115.1 ± 0.2	22.5 ± 0.2	4.8 ± 0.1	8.9 ± 0.1	4.2 ± 0.2
V68	91.6 ± 0.1	115.1 ± 0.2	23.5 ± 0.2	5.1 ± 0.1	9.9 ± 0.1	4.8 ± 0.2
Q69	93.4 ± 0.2	117.3 ± 0.2	23.9 ± 0.3	4.2 ± 0.2	9.6 ± 0.1	5.4 ± 0.2

A70	93.1 ± 0.1	115.7 ± 0.1	22.7 ± 0.2	4.6 ± 0.1	9.8 ± 0.1	5.2 ± 0.1
G71	-	-	-	-	-	-
N72	-	-	-	-	-	-
V73	93.3 ± 0.1	102.7 ± 0.1	9.5 ± 0.1	5.0 ± 0.1	3.9 ± 0.1	-1.1 ± 0.1
Q74	92.6 ± 0.1	111.0 ± 0.1	18.4 ± 0.1	4.9 ± 0.1	8.2 ± 0.1	3.2 ± 0.1
L75	93.1 ± 0.1	114.6 ± 0.1	21.5 ± 0.1	4.3 ± 0.1	9.1 ± 0.1	4.8 ± 0.1
R76	93.7 ± 0.0	94.3 ± 0.0	0.5 ± 0.1	4.9 ± 0.1	9.1 ± 0.1	4.2 ± 0.1
V77	93.2 ± 0.1	85.6 ± 0.1	-7.6 ± 0.1	4.9 ± 0.1	3.4 ± 0.1	-1.5 ± 0.1
I78	93.0 ± 0.5	84.4 ± 0.6	-8.6 ± 0.8	3.7 ± 0.4	0.6 ± 0.4	-3.1 ± 0.6
G79	92.7 ± 0.5	88.7 ± 0.5	-4.0 ± 0.6	4.6 ± 0.4	8.8 ± 0.3	4.2 ± 0.5
H80	-	-	-	-	-	-
S81	93.5 ± 0.2	78.3 ± 0.2	-15.3 ± 0.3	5.1 ± 0.2	5.8 ± 0.2	0.7 ± 0.2
M82	91.2 ± 0.4	77.9 ± 0.5	-13.3 ± 0.6	4.3 ± 0.2	0.8 ± 0.2	-3.5 ± 0.3
Q83	91.6 ± 0.2	83.4 ± 0.2	-8.2 ± 0.3	4.9 ± 0.1	3.6 ± 0.1	-1.3 ± 0.2
N84	92.9 ± 0.1	84.2 ± 0.1	-8.8 ± 0.1	4.6 ± 0.1	0.7 ± 0.1	-3.9 ± 0.1
C85	94.1 ± 0.4	89.8 ± 0.4	-4.3 ± 0.6	4.8 ± 0.3	4.5 ± 0.3	-0.3 ± 0.4
V86	91.6 ± 0.5	85.4 ± 0.5	-6.2 ± 0.8	4.5 ± 0.3	6.2 ± 0.2	1.7 ± 0.4
L87	-	-	-	-	-	-
K88	92.9 ± 0.2	75.1 ± 0.3	-17.8 ± 0.4	4.8 ± 0.2	5.1 ± 0.2	0.3 ± 0.3
L89	93.1 ± 0.2	85.6 ± 0.2	-7.5 ± 0.3	4.7 ± 0.2	0.3 ± 0.2	-4.3 ± 0.3
K90	93.0 ± 0.1	75.1 ± 0.2	-17.8 ± 0.2	4.2 ± 0.2	3.3 ± 0.1	-0.9 ± 0.2
V91	95.0 ± 0.1	84.7 ± 0.1	-10.3 ± 0.2	4.9 ± 0.1	0.1 ± 0.1	-4.8 ± 0.2
D92	93.2 ± 0.2	87.3 ± 0.2	-5.9 ± 0.2	4.0 ± 0.2	2.8 ± 0.2	-1.2 ± 0.2
T93	91.9 ± 0.1	107.5 ± 0.1	15.6 ± 0.1	3.9 ± 0.1	9.7 ± 0.1	5.9 ± 0.1
A94	93.4 ± 0.1	114.9 ± 0.1	21.5 ± 0.1	4.4 ± 0.1	5.1 ± 0.1	0.7 ± 0.1
N95	92.7 ± 0.2	91.4 ± 0.2	-1.3 ± 0.3	4.2 ± 0.3	10.7 ± 0.2	6.6 ± 0.3
P96	-	-	-	-	-	-
K97	93.4 ± 0.2	77.6 ± 0.2	-15.9 ± 0.3	5.1 ± 0.2	5.6 ± 0.2	0.5 ± 0.3
T98	93.4 ± 0.7	106.8 ± 0.8	13.4 ± 1.0	4.2 ± 0.5	5.5 ± 0.5	1.3 ± 0.7
P99	-	-	-	-	-	-
K100	91.2 ± 0.1	75.9 ± 0.1	-15.3 ± 0.1	3.8 ± 0.1	0.3 ± 0.1	-3.5 ± 0.1
Y101	93.3 ± 0.1	104.1 ± 0.1	10.8 ± 0.1	4.4 ± 0.1	1.0 ± 0.1	-3.4 ± 0.1
K102	91.6 ± 0.1	96.1 ± 0.1	4.5 ± 0.1	4.6 ± 0.1	10.7 ± 0.1	6.1 ± 0.1
F103	91.9 ± 0.1	94.7 ± 0.1	2.7 ± 0.1	4.3 ± 0.1	0.5 ± 0.1	-3.8 ± 0.1
V104	92.4 ± 0.1	84.7 ± 0.1	-7.7 ± 0.2	5.1 ± 0.2	6.2 ± 0.1	1.1 ± 0.2
R105	92.3 ± 0.1	86.4 ± 0.1	-5.9 ± 0.1	4.7 ± 0.1	2.3 ± 0.1	-2.3 ± 0.1
I106	94.0 ± 0.3	83.8 ± 0.4	-10.2 ± 0.5	4.0 ± 0.3	2.2 ± 0.2	-1.8 ± 0.3
Q107	92.0 ± 0.1	74.6 ± 0.1	-17.4 ± 0.2	4.3 ± 0.1	2.0 ± 0.1	-2.2 ± 0.2

P108	-	-	-	-	-	-
G109	93.7 ± 0.4	86.2 ± 0.4	-7.4 ± 0.6	5.1 ± 0.3	2.2 ± 0.3	-2.9 ± 0.4
Q110	93.9 ± 0.2	77.1 ± 0.2	-16.9 ± 0.3	-	-	-
T111	94.0 ± 0.2	83.1 ± 0.2	-10.9 ± 0.2	5.6 ± 0.2	2.7 ± 0.2	-2.9 ± 0.2
F112	93.6 ± 0.2	103.4 ± 0.2	9.7 ± 0.3	4.7 ± 0.2	2.2 ± 0.2	-2.5 ± 0.2
S113	92.5 ± 0.3	107.7 ± 0.3	15.2 ± 0.4	4.9 ± 0.3	11.8 ± 0.2	6.8 ± 0.4
V114	92.9 ± 0.3	96.6 ± 0.3	3.8 ± 0.4	4.9 ± 0.2	5.2 ± 0.2	0.2 ± 0.3
L115	90.9 ± 0.3	78.9 ± 0.3	-12.0 ± 0.5	5.1 ± 0.3	6.7 ± 0.2	1.6 ± 0.3
A116	94.1 ± 0.3	80.3 ± 0.4	-13.8 ± 0.5	4.2 ± 0.3	4.0 ± 0.2	-0.2 ± 0.3
C117	92.1 ± 0.6	84.6 ± 0.6	-7.5 ± 0.8	5.1 ± 0.4	-0.1 ± 0.4	-5.2 ± 0.5
Y118	91.9 ± 0.8	89.0 ± 0.8	-2.9 ± 1.1	4.2 ± 0.5	5.7 ± 0.5	1.5 ± 0.8
N119	93.0 ± 0.5	88.9 ± 0.5	-4.1 ± 0.8	5.8 ± 0.4	0.2 ± 0.4	-5.6 ± 0.5
G120	93.5 ± 0.4	107.7 ± 0.4	14.2 ± 0.6	5.9 ± 0.2	5.2 ± 0.3	-0.7 ± 0.4
S121	93.2 ± 0.3	95.1 ± 0.3	1.8 ± 0.4	4.7 ± 0.2	7.8 ± 0.2	3.1 ± 0.3
P122	-	-	-	-	-	-
S123	88.3 ± 1.3	82.0 ± 1.4	-6.3 ± 1.9	5.0 ± 0.9	6.4 ± 0.6	1.4 ± 1.1
G124	92.4 ± 1.0	80.2 ± 1.1	-12.2 ± 1.4	3.5 ± 1.1	0.5 ± 1.1	-3.0 ± 1.6
V125	91.7 ± 0.4	77.9 ± 0.4	-13.9 ± 0.6	4.6 ± 0.3	1.4 ± 0.3	-3.1 ± 0.4
Y126	93.4 ± 0.4	87.5 ± 0.4	-6.0 ± 0.6	4.8 ± 0.4	0.3 ± 0.3	-4.5 ± 0.5
Q127	91.3 ± 0.1	87.7 ± 0.2	-3.6 ± 0.2	4.3 ± 0.2	6.5 ± 0.1	2.2 ± 0.2
C128	93.4 ± 0.5	108.1 ± 0.5	14.7 ± 0.7	4.9 ± 0.3	3.7 ± 0.2	-1.2 ± 0.4
A129	91.6 ± 0.1	99.3 ± 0.1	7.7 ± 0.2	4.6 ± 0.2	9.3 ± 0.1	4.7 ± 0.2
M130	94.0 ± 0.2	87.8 ± 0.2	-6.1 ± 0.3	4.2 ± 0.2	3.6 ± 0.2	-0.6 ± 0.2
R131	95.2 ± 0.4	90.2 ± 0.4	-5.1 ± 0.5	5.6 ± 0.2	2.5 ± 0.2	-3.1 ± 0.3
P132	-	-	-	-	-	-
N133	92.0 ± 0.4	81.3 ± 0.4	-10.7 ± 0.6	4.9 ± 0.3	3.1 ± 0.3	-1.8 ± 0.4
F134	94.5 ± 0.4	81.5 ± 0.4	-13.0 ± 0.6	4.9 ± 0.3	1.5 ± 0.3	-3.4 ± 0.4
T135	92.4 ± 0.7	105.4 ± 0.7	13.0 ± 1.0	4.1 ± 0.4	7.3 ± 0.4	3.2 ± 0.6
I136	95.2 ± 1.1	89.6 ± 1.1	-5.7 ± 1.6	4.1 ± 0.6	4.4 ± 0.6	0.3 ± 0.8
K137	92.6 ± 0.7	81.5 ± 0.7	-11.1 ± 1.0	5.5 ± 0.5	1.7 ± 0.4	-3.8 ± 0.6
G138	95.4 ± 0.4	77.5 ± 0.5	-17.8 ± 0.7	5.8 ± 0.3	3.4 ± 0.3	-2.4 ± 0.4
S139	91.6 ± 0.8	101.7 ± 0.9	10.0 ± 1.2	4.5 ± 0.5	10.8 ± 0.4	6.3 ± 0.7
F140	93.1 ± 0.3	111.9 ± 0.4	18.8 ± 0.5	5.2 ± 0.3	3.2 ± 0.3	-2.0 ± 0.4
L141	93.5 ± 0.6	104.9 ± 0.6	11.3 ± 0.8	4.1 ± 0.5	10.6 ± 0.4	6.5 ± 0.6
N142	-	-	-	-	-	-
G143	-	-	-	-	-	-
S144	93.1 ± 1.6	114.8 ± 2.1	21.7 ± 2.6	3.4 ± 1.3	12.0 ± 1.1	8.7 ± 1.7
A145	96.4 ± 1.0	87.8 ± 1.0	-8.6 ± 1.4	5.2 ± 0.4	0.8 ± 0.4	-4.4 ± 0.6

G146	93.7 ± 1.4	103.6 ± 1.5	9.9 ± 2.0	5.6 ± 0.8	2.0 ± 0.7	-3.6 ± 1.1
S147	88.6 ± 0.9	96.9 ± 0.9	8.3 ± 1.3	3.8 ± 0.5	7.6 ± 0.5	3.8 ± 0.7
V148	-	-	-	-	-	-
G149	92.2 ± 0.7	79.3 ± 0.7	-13.0 ± 1.0	3.6 ± 0.4	0.6 ± 0.4	-3.0 ± 0.6
F150	92.3 ± 0.4	90.6 ± 0.4	-1.8 ± 0.5	4.5 ± 0.3	0.3 ± 0.3	-4.2 ± 0.4
N151	91.1 ± 0.1	97.4 ± 0.1	6.2 ± 0.2	3.7 ± 0.2	5.1 ± 0.1	1.4 ± 0.2
I152	-	-	-	-	-	-
D153	93.0 ± 0.1	102.8 ± 0.2	9.8 ± 0.2	4.5 ± 0.2	8.4 ± 0.1	3.9 ± 0.2
Y154	93.5 ± 0.2	105.6 ± 0.2	12.2 ± 0.3	4.8 ± 0.3	2.6 ± 0.2	-2.2 ± 0.4
D155	92.2 ± 0.3	87.0 ± 0.3	-5.2 ± 0.4	5.0 ± 0.3	4.4 ± 0.2	-0.6 ± 0.4
C156	93.0 ± 0.1	103.0 ± 0.1	10.0 ± 0.2	5.0 ± 0.2	9.4 ± 0.1	4.4 ± 0.2
V157	91.6 ± 0.1	111.7 ± 0.2	20.1 ± 0.2	4.4 ± 0.1	5.6 ± 0.1	1.2 ± 0.2
S158	92.6 ± 0.2	91.7 ± 0.2	-1.0 ± 0.2	4.6 ± 0.2	11.0 ± 0.1	6.5 ± 0.2
F159	92.6 ± 0.1	102.3 ± 0.1	9.7 ± 0.2	4.4 ± 0.1	4.5 ± 0.1	0.2 ± 0.2
C160	90.6 ± 0.7	77.4 ± 0.8	-13.2 ± 1.1	5.0 ± 0.8	5.9 ± 0.7	0.9 ± 1.0
Y161	92.1 ± 0.7	91.0 ± 0.8	-1.1 ± 1.1	4.6 ± 0.5	3.3 ± 0.4	-1.3 ± 0.7
M162	92.2 ± 0.3	90.3 ± 0.3	-1.8 ± 0.4	4.5 ± 0.2	0.5 ± 0.2	-3.9 ± 0.3
H163	91.8 ± 0.8	91.0 ± 0.8	-0.8 ± 1.1	3.4 ± 0.8	0.9 ± 1.1	-2.5 ± 1.3
H164	-	-	-	-	-	-
M165	-	-	-	-	-	-
E166	93.3 ± 0.2	85.3 ± 0.2	-8.0 ± 0.3	4.3 ± 0.3	1.7 ± 0.2	-2.6 ± 0.3
L167	94.5 ± 0.2	78.4 ± 0.2	-16.1 ± 0.2	4.4 ± 0.1	4.2 ± 0.1	-0.2 ± 0.2
P168	-	-	-	-	-	-
T169	-	-	-	-	-	-
G170	94.2 ± 0.2	85.5 ± 0.2	-8.6 ± 0.3	5.2 ± 0.2	9.5 ± 0.2	4.3 ± 0.2
V171	93.7 ± 1.0	77.9 ± 1.2	-15.8 ± 1.6	3.4 ± 0.4	0.6 ± 0.4	-2.8 ± 0.6
H172	94.6 ± 0.9	78.9 ± 1.0	-15.6 ± 1.4	5.3 ± 0.5	1.4 ± 0.5	-3.9 ± 0.7
A173	92.8 ± 0.4	90.0 ± 0.4	-2.8 ± 0.6	5.5 ± 0.3	5.7 ± 0.3	0.2 ± 0.5
G174	91.9 ± 0.8	98.0 ± 0.8	6.1 ± 1.2	4.3 ± 0.5	1.9 ± 0.5	-2.5 ± 0.7
T175	92.5 ± 1.0	93.5 ± 1.0	1.0 ± 1.4	4.4 ± 0.5	10.3 ± 0.4	5.8 ± 0.6
D176	90.8 ± 0.3	76.0 ± 0.3	-14.8 ± 0.4	3.6 ± 0.2	0.8 ± 0.2	-2.8 ± 0.3
L177	92.9 ± 0.7	82.2 ± 0.8	-10.7 ± 1.1	6.2 ± 0.5	4.0 ± 0.4	-2.1 ± 0.7
E178	90.8 ± 0.8	104.5 ± 0.9	13.6 ± 1.2	4.1 ± 0.5	9.0 ± 0.5	4.8 ± 0.7
G179	95.2 ± 0.8	80.6 ± 0.8	-14.6 ± 1.1	5.0 ± 0.6	3.9 ± 0.6	-1.1 ± 0.8
N180	94.2 ± 0.3	81.4 ± 0.3	-12.8 ± 0.4	4.7 ± 0.2	1.0 ± 0.2	-3.7 ± 0.3
F181	94.2 ± 0.2	75.5 ± 0.2	-18.7 ± 0.3	4.5 ± 0.2	2.2 ± 0.2	-2.3 ± 0.3
Y182	92.0 ± 0.2	85.7 ± 0.2	-6.2 ± 0.3	3.9 ± 0.2	0.6 ± 0.2	-3.3 ± 0.2
G183	94.4 ± 0.1	89.1 ± 0.1	-5.3 ± 0.1	5.1 ± 0.1	2.8 ± 0.1	-2.3 ± 0.2

P184	-	-	-	-	-	-
F185	-	-	-	-	-	-
V186	90.9 ± 0.2	102.6 ± 0.3	11.7 ± 0.4	4.4 ± 0.2	2.0 ± 0.2	-2.4 ± 0.3
D187	93.2 ± 0.2	95.0 ± 0.2	1.8 ± 0.3	5.8 ± 0.2	11.3 ± 0.1	5.4 ± 0.2
R188	-	-	-	3.6 ± 0.2	10.8 ± 0.2	7.2 ± 0.2
Q189	93.7 ± 0.1	95.7 ± 0.1	2.0 ± 0.1	4.6 ± 0.1	2.4 ± 0.1	-2.2 ± 0.2
T190	93.4 ± 0.1	82.8 ± 0.1	-10.6 ± 0.1	4.5 ± 0.1	1.8 ± 0.1	-2.7 ± 0.1
A191	-	-	-	-	-	-
Q192	91.6 ± 0.1	87.2 ± 0.1	-4.4 ± 0.2	4.8 ± 0.1	2.2 ± 0.1	-2.6 ± 0.1
A193	91.2 ± 0.1	81.2 ± 0.1	-10.0 ± 0.2	4.6 ± 0.2	3.3 ± 0.1	-1.3 ± 0.2
A194	91.4 ± 0.1	89.3 ± 0.1	-2.1 ± 0.1	4.3 ± 0.1	1.9 ± 0.1	-2.4 ± 0.1
G195	94.0 ± 0.1	109.3 ± 0.1	15.3 ± 0.2	4.7 ± 0.1	5.2 ± 0.1	0.5 ± 0.1
T196	91.0 ± 0.3	84.1 ± 0.3	-6.9 ± 0.4	4.2 ± 0.4	6.7 ± 0.2	2.5 ± 0.5
D197	92.6 ± 0.1	95.0 ± 0.1	2.4 ± 0.2	4.4 ± 0.1	2.3 ± 0.1	-2.1 ± 0.1
T198	92.2 ± 0.1	112.2 ± 0.1	20.0 ± 0.1	4.2 ± 0.1	6.3 ± 0.1	2.1 ± 0.1
T199	92.1 ± 0.2	111.9 ± 0.3	19.7 ± 0.4	4.1 ± 0.2	8.3 ± 0.1	4.2 ± 0.2
I200	90.4 ± 0.2	85.9 ± 0.2	-4.5 ± 0.3	4.2 ± 0.2	5.5 ± 0.2	1.4 ± 0.2
T201	92.6 ± 0.5	81.6 ± 0.5	-11.0 ± 0.7	3.3 ± 0.4	3.7 ± 0.4	0.4 ± 0.5
V202	92.0 ± 0.2	75.1 ± 0.3	-16.9 ± 0.4	4.8 ± 0.2	5.4 ± 0.2	0.6 ± 0.3
N203	92.4 ± 0.5	76.3 ± 0.6	-16.1 ± 0.8	3.9 ± 0.4	0.6 ± 0.4	-3.4 ± 0.6
V204	92.1 ± 0.8	77.2 ± 1.0	-14.9 ± 1.3	4.4 ± 0.6	5.4 ± 0.6	1.0 ± 0.9
L205	93.2 ± 0.5	74.5 ± 0.7	-18.6 ± 0.8	3.8 ± 0.8	2.6 ± 0.8	-1.2 ± 1.2
A206	-	-	-	5.1 ± 0.6	3.6 ± 0.6	-1.4 ± 0.8
W207	94.0 ± 0.5	77.8 ± 0.6	-16.3 ± 0.7	4.4 ± 0.3	2.7 ± 0.4	-1.7 ± 0.5
L208	-	-	-	-	-	-
Y209	94.2 ± 1.0	78.1 ± 1.1	-16.0 ± 1.5	5.4 ± 0.6	4.8 ± 0.5	-0.7 ± 0.8
A210	-	-	-	4.2 ± 1.2	0.5 ± 1.2	-3.7 ± 1.7
A211	93.6 ± 0.6	76.6 ± 0.7	-16.9 ± 0.9	4.7 ± 0.5	6.8 ± 0.4	2.1 ± 0.7
V212	93.4 ± 0.5	75.9 ± 0.5	-17.5 ± 0.7	4.4 ± 0.4	1.6 ± 0.4	-2.8 ± 0.5
I213	94.4 ± 0.4	76.2 ± 0.5	-18.1 ± 0.6	5.2 ± 0.5	5.2 ± 0.4	-0.0 ± 0.6
N214	92.7 ± 0.5	78.7 ± 0.6	-14.0 ± 0.8	4.7 ± 0.5	2.5 ± 0.5	-2.2 ± 0.7
G215	93.2 ± 0.3	85.5 ± 0.3	-7.6 ± 0.4	4.5 ± 0.3	3.1 ± 0.2	-1.4 ± 0.4
D216	93.0 ± 0.2	102.5 ± 0.2	9.5 ± 0.3	4.6 ± 0.2	1.9 ± 0.2	-2.7 ± 0.2
R217	89.3 ± 0.3	79.6 ± 0.3	-9.7 ± 0.5	3.9 ± 0.4	5.9 ± 0.4	2.0 ± 0.6
W218	-	-	-	4.3 ± 1.2	0.0 ± 0.9	-4.3 ± 1.5
F219	-	-	-	-	-	-
L220	93.1 ± 0.1	81.4 ± 0.1	-11.7 ± 0.1	4.7 ± 0.1	1.3 ± 0.1	-3.3 ± 0.2
N221	92.7 ± 0.1	94.2 ± 0.1	1.6 ± 0.2	4.6 ± 0.2	0.8 ± 0.2	-3.9 ± 0.3

R222	-	-	-	-	-	-
F223	93.3 ± 0.1	90.8 ± 0.1	-2.5 ± 0.1	4.4 ± 0.1	2.4 ± 0.1	-2.1 ± 0.1
T224	92.0 ± 0.0	106.3 ± 0.1	14.2 ± 0.1	4.8 ± 0.1	4.3 ± 0.0	-0.5 ± 0.1
T225	93.0 ± 0.0	109.4 ± 0.1	16.4 ± 0.1	4.0 ± 0.1	9.8 ± 0.0	5.8 ± 0.1
T226	92.5 ± 0.2	97.6 ± 0.2	5.1 ± 0.3	3.5 ± 0.3	1.4 ± 0.2	-2.1 ± 0.3
L227	92.9 ± 0.2	87.6 ± 0.2	-5.3 ± 0.3	5.6 ± 0.3	7.6 ± 0.2	2.0 ± 0.4
N228	93.4 ± 0.4	85.4 ± 0.4	-8.1 ± 0.5	5.3 ± 0.6	3.3 ± 0.4	-2.0 ± 0.7
D229	94.8 ± 0.3	83.6 ± 0.3	-11.2 ± 0.4	5.1 ± 0.3	1.0 ± 0.3	-4.1 ± 0.4
F230	94.5 ± 0.2	91.0 ± 0.2	-3.5 ± 0.2	5.0 ± 0.2	8.2 ± 0.2	3.3 ± 0.3
N231	94.7 ± 0.2	87.9 ± 0.2	-6.7 ± 0.3	4.8 ± 0.2	3.7 ± 0.2	-1.1 ± 0.3
L232	94.5 ± 0.2	82.1 ± 0.2	-12.5 ± 0.2	5.2 ± 0.2	5.8 ± 0.2	0.7 ± 0.3
V233	93.8 ± 0.3	87.4 ± 0.3	-6.4 ± 0.5	4.4 ± 0.3	0.7 ± 0.4	-3.6 ± 0.5
A234	-	-	-	-	-	-
M235	94.4 ± 0.2	87.4 ± 0.2	-7.0 ± 0.3	4.0 ± 0.2	3.5 ± 0.2	-0.5 ± 0.3
K236	94.0 ± 0.2	80.0 ± 0.2	-14.0 ± 0.3	4.5 ± 0.3	4.3 ± 0.2	-0.3 ± 0.4
Y237	91.6 ± 0.3	87.2 ± 0.3	-4.3 ± 0.4	4.9 ± 0.4	5.8 ± 0.4	0.9 ± 0.5
N238	93.9 ± 0.2	95.9 ± 0.2	2.1 ± 0.3	4.5 ± 0.2	1.0 ± 0.2	-3.5 ± 0.3
Y239	91.7 ± 0.3	105.3 ± 0.4	13.6 ± 0.5	4.8 ± 0.2	4.3 ± 0.2	-0.4 ± 0.3
E240	94.5 ± 0.2	90.8 ± 0.2	-3.7 ± 0.3	4.5 ± 0.2	9.3 ± 0.2	4.7 ± 0.3
P241	-	-	-	-	-	-
L242	92.3 ± 0.1	116.1 ± 0.2	23.8 ± 0.3	4.4 ± 0.1	6.2 ± 0.1	1.7 ± 0.2
T243	92.1 ± 0.1	100.7 ± 0.1	8.5 ± 0.2	4.2 ± 0.1	11.1 ± 0.1	6.9 ± 0.2
Q244	91.4 ± 0.4	79.2 ± 0.5	-12.2 ± 0.6	4.3 ± 0.5	2.0 ± 0.3	-2.3 ± 0.6
D245	92.9 ± 0.2	79.6 ± 0.2	-13.3 ± 0.3	5.2 ± 0.2	0.4 ± 0.2	-4.7 ± 0.3
H246	92.9 ± 0.2	93.2 ± 0.2	0.3 ± 0.3	5.1 ± 0.3	8.8 ± 0.3	3.7 ± 0.4
V247	91.6 ± 0.2	80.1 ± 0.2	-11.5 ± 0.3	4.4 ± 0.2	5.1 ± 0.2	0.7 ± 0.3
D248	93.1 ± 0.2	76.9 ± 0.2	-16.2 ± 0.3	4.5 ± 0.2	1.5 ± 0.2	-3.1 ± 0.3
I249	94.3 ± 0.4	84.5 ± 0.5	-9.8 ± 0.6	4.5 ± 0.4	0.8 ± 0.3	-3.7 ± 0.5
L250	-	-	-	-	-	-
G251	94.5 ± 0.2	80.5 ± 0.2	-14.0 ± 0.3	4.7 ± 0.2	2.6 ± 0.2	-2.1 ± 0.3
P252	-	-	-	-	-	-
L253	92.3 ± 0.4	77.1 ± 0.5	-15.2 ± 0.6	4.8 ± 0.3	2.4 ± 0.4	-2.4 ± 0.5
S254	93.3 ± 0.5	84.1 ± 0.5	-9.2 ± 0.7	5.0 ± 0.3	0.6 ± 0.4	-4.4 ± 0.5
A255	92.9 ± 0.2	86.8 ± 0.2	-6.1 ± 0.3	4.4 ± 0.2	9.8 ± 0.2	5.4 ± 0.3
Q256	94.1 ± 0.3	79.4 ± 0.3	-14.7 ± 0.5	4.7 ± 0.3	2.6 ± 0.3	-2.1 ± 0.4
T257	91.8 ± 1.4	75.5 ± 1.6	-16.2 ± 2.1	3.9 ± 1.2	1.5 ± 1.3	-2.4 ± 1.8
G258	94.7 ± 0.4	103.9 ± 0.5	9.2 ± 0.6	4.7 ± 0.3	3.2 ± 0.4	-1.5 ± 0.5
I259	93.1 ± 0.2	108.6 ± 0.3	15.5 ± 0.4	5.0 ± 0.2	3.7 ± 0.2	-1.3 ± 0.3

A260	93.2 ± 0.2	101.5 ± 0.2	8.3 ± 0.3	5.0 ± 0.2	8.2 ± 0.1	3.2 ± 0.3
V261	93.5 ± 0.1	101.1 ± 0.1	7.6 ± 0.2	4.7 ± 0.1	5.9 ± 0.1	1.2 ± 0.2
L262	93.8 ± 0.2	91.1 ± 0.2	-2.8 ± 0.3	5.1 ± 0.2	2.9 ± 0.2	-2.2 ± 0.3
D263	92.3 ± 0.4	108.6 ± 0.4	16.3 ± 0.6	4.1 ± 0.3	3.3 ± 0.3	-0.8 ± 0.5
M264	94.9 ± 0.4	102.4 ± 0.4	7.5 ± 0.6	4.3 ± 0.5	12.0 ± 0.4	7.7 ± 0.6
C265	93.3 ± 0.6	95.3 ± 0.6	2.0 ± 0.8	4.0 ± 0.4	1.9 ± 0.5	-2.1 ± 0.6
A266	94.5 ± 0.3	90.8 ± 0.3	-3.8 ± 0.4	4.7 ± 0.2	1.2 ± 0.3	-3.5 ± 0.3
S267	93.9 ± 0.4	103.7 ± 0.5	9.8 ± 0.6	3.9 ± 0.5	9.4 ± 0.5	5.5 ± 0.7
L268	94.0 ± 0.2	97.5 ± 0.2	3.5 ± 0.3	4.8 ± 0.3	7.3 ± 0.2	2.5 ± 0.4
K269	94.8 ± 0.3	89.6 ± 0.3	-5.2 ± 0.4	4.1 ± 0.3	1.9 ± 0.3	-2.2 ± 0.4
E270	93.8 ± 0.3	92.6 ± 0.3	-1.2 ± 0.4	4.4 ± 0.4	0.6 ± 0.3	-3.8 ± 0.5
L271	93.1 ± 0.3	99.4 ± 0.3	6.3 ± 0.4	4.7 ± 0.5	11.6 ± 0.3	6.9 ± 0.6
L272	94.8 ± 0.4	91.4 ± 0.4	-3.4 ± 0.6	4.8 ± 0.4	2.7 ± 0.4	-2.1 ± 0.6
Q273	94.0 ± 0.3	85.9 ± 0.3	-8.0 ± 0.4	5.5 ± 0.5	1.6 ± 0.4	-4.0 ± 0.7
N274	92.8 ± 0.3	99.3 ± 0.3	6.5 ± 0.5	4.5 ± 0.5	3.1 ± 0.4	-1.4 ± 0.6
G275	93.9 ± 0.2	93.2 ± 0.2	-0.7 ± 0.2	4.7 ± 0.3	10.1 ± 0.2	5.4 ± 0.4
M276	92.4 ± 0.2	80.3 ± 0.2	-12.1 ± 0.3	5.1 ± 0.4	3.6 ± 0.2	-1.4 ± 0.5
N277	91.2 ± 0.8	75.9 ± 1.0	-15.3 ± 1.3	2.5 ± 1.7	4.0 ± 0.6	1.5 ± 1.8
G278	94.0 ± 0.3	80.3 ± 0.4	-13.7 ± 0.5	4.7 ± 0.6	6.0 ± 0.3	1.2 ± 0.6
R279	91.8 ± 0.1	85.7 ± 0.1	-6.1 ± 0.1	4.2 ± 0.1	1.5 ± 0.1	-2.7 ± 0.2
T280	93.5 ± 0.1	74.6 ± 0.1	-18.8 ± 0.2	5.2 ± 0.2	2.6 ± 0.2	-2.6 ± 0.3
I281	93.2 ± 0.9	79.9 ± 1.0	-13.3 ± 1.3	3.9 ± 0.8	4.1 ± 0.6	0.2 ± 1.0
L282	-	-	-	-	-	-
G283	92.5 ± 1.2	96.6 ± 1.2	4.2 ± 1.7	5.3 ± 0.8	9.8 ± 0.6	4.5 ± 0.9
S284	-	-	-	-	-	-
A285	92.0 ± 0.7	88.8 ± 0.7	-3.3 ± 1.0	5.7 ± 0.6	0.4 ± 0.5	-5.3 ± 0.7
L286	90.2 ± 0.4	103.6 ± 0.4	13.4 ± 0.5	-	-	-
L287	-	-	-	-	-	-
E288	-	-	-	-	-	-
D289	-	-	-	5.2 ± 0.5	1.5 ± 0.6	-3.7 ± 0.8
E290	91.0 ± 0.6	92.3 ± 0.6	1.3 ± 0.8	3.8 ± 0.4	0.6 ± 0.5	-3.2 ± 0.6
F291	91.9 ± 1.2	114.9 ± 1.6	22.9 ± 2.0	4.8 ± 0.6	6.7 ± 0.6	1.9 ± 0.8
T292	93.2 ± 0.2	111.0 ± 0.3	17.8 ± 0.4	4.8 ± 0.2	11.8 ± 0.2	7.0 ± 0.3
P293	-	-	-	-	-	-
F294	92.9 ± 0.2	73.8 ± 0.3	-19.1 ± 0.3	5.0 ± 0.2	2.0 ± 0.2	-3.0 ± 0.3
D295	-	-	-	-	-	-
V296	92.3 ± 0.4	81.6 ± 0.5	-10.7 ± 0.6	3.9 ± 0.4	6.7 ± 0.4	2.7 ± 0.5
V297	91.5 ± 0.9	76.2 ± 1.0	-15.3 ± 1.4	4.2 ± 0.4	1.2 ± 0.5	-3.0 ± 0.6

R298	94.0 ± 0.5	77.9 ± 0.6	-16.1 ± 0.8	5.0 ± 0.3	0.7 ± 0.4	-4.3 ± 0.5
Q299	94.1 ± 0.6	90.1 ± 0.6	-4.0 ± 0.8	5.1 ± 0.6	9.3 ± 0.5	4.2 ± 0.7
C300	91.6 ± 0.9	79.7 ± 1.0	-11.9 ± 1.3	4.8 ± 0.6	3.8 ± 0.6	-1.1 ± 0.9
S301	90.9 ± 1.0	76.8 ± 1.2	-14.1 ± 1.6	3.6 ± 0.7	2.6 ± 0.6	-1.0 ± 0.9
G302	94.8 ± 0.4	95.4 ± 0.4	0.6 ± 0.6	4.8 ± 0.3	3.0 ± 0.2	-1.8 ± 0.3
V303	92.3 ± 0.1	99.1 ± 0.1	6.8 ± 0.1	4.2 ± 0.1	4.4 ± 0.1	0.3 ± 0.1
T304	93.3 ± 0.1	89.9 ± 0.1	-3.4 ± 0.1	4.5 ± 0.1	5.7 ± 0.0	1.2 ± 0.1
F305	92.2 ± 0.2	88.0 ± 0.2	-4.1 ± 0.2	4.4 ± 0.2	3.6 ± 0.1	-0.8 ± 0.2
Q306	91.5 ± 0.0	87.1 ± 0.0	-4.4 ± 0.0	4.2 ± 0.0	3.3 ± 0.0	-0.9 ± 0.0

Table S3: Assessment of X-ray and AlphaFold2 structure quality using 254 $^1\text{D}_{\text{NH}}$ and 257 $^2\text{D}_{\text{C}\text{H}}$ RDCs. Rows are colored by AlphaFold2 implementation, for the *full* (blue; AF subscript), date-limited (orange; AFD subscript), and *sequence-limited* (green; AFS subscript). C^α RMSD values are relative to the ‘consensus’ PDB structure PDB: 5R8T. Five different subsections of the data are presented: (All) – all residues used to determine the alignment tensor. (Incl.) - residues 5-115 and 199-272, used to determine the alignment tensor, which was also used for the SVD fit of (Excl.) residues 2-5, 116-198, and 273-301, using the same alignment tensor. Similarly (SS) – residues in secondary structure (as defined in PDB 5R8T) – were used to determine the alignment tensor, which was used for the SVD fit of (non-SS) residues outside well-defined secondary structure. The ‘Amber relaxed’ column reports whether the final Amber relaxation step has been applied to the model. The average per-residue predicted local-distance difference test (pLDDT) scores are also reported for each model; this average is used to rank each model.

Model	Amber relaxed	Ca RMSD	pLDDT	Q (All)	Q (Incl.)	Q (Excl.)	Q (SS)	Q (non-SS)	ΔD NH (All)	ΔD NH (Incl.)	ΔD NH (Excl.)	ΔD NH (SS)	ΔD NH (non-SS)	ΔD C' H (All)	ΔD C' H (Incl.)	ΔD C' H (Excl.)	ΔD C' H (SS)	ΔD C' H (non-SS)
5R8T	N/A	N/A	N/A	0.284	0.208	0.356	0.249	0.328	3.272	2.329	4.323	2.761	4.060	1.023	0.791	1.249	0.956	1.136
M^{pro}_AF1	FALSE	0.408	95.46	0.285	0.213	0.360	0.223	0.346	3.163	2.367	4.084	2.487	4.123	1.043	0.794	1.316	0.866	1.266
M^{pro}_AF1	TRUE	0.406	95.46	0.280	0.220	0.341	0.234	0.329	3.152	2.521	3.918	2.712	3.841	1.024	0.807	1.246	0.872	1.219
M^{pro}_AFD1	FALSE	0.644	94.97	0.313	0.226	0.348	0.227	0.390	3.306	2.524	3.775	2.572	4.419	1.138	0.823	1.301	0.858	1.471
M^{pro}_AFD1	TRUE	0.644	94.97	0.322	0.248	0.337	0.262	0.373	3.608	2.902	3.933	3.099	4.487	1.114	0.878	1.196	0.945	1.322
M^{pro}_AFS1	FALSE	1.015	91.66	0.463	0.282	0.616	0.287	0.616	4.846	3.195	6.430	3.179	6.696	1.614	0.984	2.307	1.042	2.271
M^{pro}_AFS1	TRUE	1.023	91.66	0.441	0.300	0.577	0.310	0.562	4.774	3.459	6.332	3.475	6.365	1.516	1.022	2.068	1.108	1.987
M^{pro}_AF2	FALSE	0.406	95.17	0.280	0.212	0.352	0.220	0.339	3.130	2.345	4.059	2.454	4.101	1.018	0.789	1.270	0.853	1.222
M^{pro}_AF2	TRUE	0.406	95.17	0.283	0.218	0.346	0.233	0.331	3.213	2.496	4.052	2.711	3.995	1.014	0.798	1.244	0.873	1.189
M^{pro}_AFD2	FALSE	0.640	94.90	0.310	0.226	0.336	0.228	0.384	3.323	2.537	3.693	2.578	4.463	1.113	0.822	1.250	0.862	1.415
M^{pro}_AFD2	TRUE	0.640	94.90	0.323	0.240	0.342	0.258	0.378	3.619	2.793	3.943	3.050	4.584	1.113	0.856	1.232	0.934	1.333
M^{pro}_AFS2	FALSE	1.256	90.86	0.506	0.325	0.650	0.289	0.672	5.199	3.701	6.644	3.089	7.395	1.735	1.102	2.426	1.095	2.484
M^{pro}_AFS2	TRUE	1.258	90.86	0.451	0.313	0.559	0.305	0.584	4.856	3.541	6.215	3.312	6.625	1.566	1.102	1.995	1.140	2.104
M^{pro}_AF3	FALSE	1.074	91.45	0.453	0.283	0.599	0.290	0.599	4.826	3.194	6.407	3.170	6.653	1.562	0.991	2.192	1.058	2.152
M^{pro}_AF3	TRUE	1.084	91.45	0.430	0.301	0.551	0.312	0.546	4.756	3.452	6.140	3.477	6.286	1.465	1.031	1.942	1.119	1.894
M^{pro}_AFD3	FALSE	1.004	91.50	0.455	0.276	0.604	0.283	0.606	4.766	3.127	6.259	3.119	6.586	1.599	0.973	2.288	1.036	2.245
M^{pro}_AFD3	TRUE	1.012	91.50	0.435	0.292	0.573	0.302	0.559	4.669	3.357	6.180	3.380	6.224	1.530	1.011	2.109	1.093	2.033
M^{pro}_AFS3	FALSE	1.093	90.84	0.419	0.296	0.533	0.284	0.544	4.691	3.437	6.056	3.089	6.387	1.414	1.009	1.857	1.063	1.902
M^{pro}_AFS3	TRUE	1.100	90.84	0.407	0.300	0.509	0.294	0.516	4.536	3.441	5.888	3.296	6.025	1.394	1.047	1.761	1.079	1.821
M^{pro}_AF4	FALSE	1.073	90.67	0.453	0.288	0.584	0.261	0.609	4.617	3.277	5.753	2.793	6.539	1.618	1.005	2.279	1.000	2.333
M^{pro}_AF4	TRUE	1.071	90.67	0.434	0.280	0.549	0.272	0.572	4.550	3.124	5.804	2.996	6.248	1.544	1.011	2.068	1.027	2.175
M^{pro}_AFD4	FALSE	1.395	90.00	0.475	0.300	0.614	0.287	0.628	4.871	3.309	6.158	2.982	6.951	1.670	1.063	2.344	1.113	2.331
M^{pro}_AFD4	TRUE	1.398	90.00	0.462	0.311	0.587	0.287	0.611	4.856	3.416	6.241	3.047	6.882	1.614	1.116	2.156	1.100	2.229
M^{pro}_AFS4	FALSE	1.130	90.41	0.468	0.294	0.611	0.271	0.629	4.793	3.213	6.332	2.905	6.799	1.651	1.056	2.293	1.030	2.372
M^{pro}_AFS4	TRUE	1.131	90.41	0.431	0.298	0.547	0.288	0.565	4.548	3.270	5.922	3.109	6.179	1.539	1.073	1.998	1.082	2.102
M^{pro}_AF5	FALSE	1.390	89.84	0.478	0.325	0.608	0.324	0.626	4.974	3.639	6.074	3.471	6.613	1.653	1.120	2.302	1.178	2.306
M^{pro}_AF5	TRUE	1.403	89.84	0.453	0.357	0.546	0.347	0.572	4.883	4.014	5.620	3.727	6.248	1.573	1.229	2.028	1.258	2.043
M^{pro}_AFD5	FALSE	1.318	89.85	0.484	0.317	0.632	0.315	0.635	5.039	3.499	6.524	3.382	6.828	1.669	1.109	2.339	1.156	2.329
M^{pro}_AFD5	TRUE	1.328	89.85	0.430	0.324	0.538	0.339	0.532	4.678	3.583	5.733	3.666	5.868	1.500	1.142	1.954	1.225	1.896
M^{pro}_AFS5	FALSE	1.394	89.71	0.482	0.319	0.618	0.319	0.631	5.082	3.526	6.491	3.441	6.857	1.642	1.116	2.259	1.160	2.288
M^{pro}_AFS5	TRUE	1.404	89.71	0.439	0.331	0.540	0.345	0.541	4.797	3.689	5.823	3.737	6.045	1.504	1.152	1.939	1.246	1.900

Table S4: PDB structures chosen by the AlphaFold2 algorithm as a diverse set of templates from pdb70 with varying sequence homology to the target protein (in our case M^{pro}). These PDB files then act as input to the AlphaFold2 neural network. We note that PDB entry 2LIZ is an NMR structure ensemble of the C-terminal helical domain (2.5M urea). Furthermore, PDB entry 3EBN is a crystal structure of the C-terminal domain (domain 3) as a domain-swapped dimer.

Full			Date-limited			Sequence-limited		
PD B	C hain	Organism/ protein	PD B	C hain	Organism/ protein	PD B	C hain	Organism/ protein
3S ND	A	SARS-CoV-1 / Mpro	3S ND	A	SARS-CoV-1 / Mpro	4H AN	A	Human / Galectin-8
6Y B7	A	SARS-CoV-2 / Mpro	2Y NA	A	Tylonycteris bat CoV HKU4 / Mpro	2M P3	A	Human / Superoxide dismutase
2Y NA	A	Tylonycteris bat CoV HKU4 / Mpro	4W ME	D	MERS-CoV / Mpro	3K BE	A	<i>Caenorhabditis elegans</i> / Superoxide dismutase
4W ME	D	MERS-CoV / Mpro	5H YO	A	Porcine epidemic diarrhea virus (CoV) / Mpro	2IJ D	A	Human poliovirus 1 / Picornain 3C RNA-directed RNA polymerase
5H YO	A	Porcine epidemic diarrhea virus (CoV) / Mpro	3T LO	A	Human CoV NL63 / Mpro	3M MG	A	Tobacco vein mottling virus / Nuclear inclusion protein A
3T LO	A	Human CoV NL63 / Mpro	1L VO	B	Transmissible gastroenteritis CoV / Replicase hydrolase domain	1L VM	A	Tobacco etch virus / Catalytic domain of the nuclear inclusion protein A
1L VO	B	Transmissible gastroenteritis CoV / Replicase hydrolase domain	3D 23	D	Human CoV HKU1 / Mpro	1L VM	B	Tobacco etch virus / Catalytic domain of the nuclear inclusion protein A
3D 23	D	Human CoV HKU1 / Mpro	4Z RO	A	Feline CoV / Mpro	5H XF	A	Enterovirus A71 / Mpro
4Z RO	A	Feline CoV / Mpro	5N H0	B	Human CoV NL63 / Mpro	4X LG	B	<i>Candida glabrata</i> / Structure-specific endonuclease subunit SLX1
5N H0	B	Human CoV NL63 / Mpro	4X FQ	A	Porcine epidemic diarrhea virus (CoV) / Mpro	1W SU	D	<i>Moarella thermoacetica</i> / Selenocysteine-specific elongation factor
4X FQ	A	Porcine epidemic diarrhea virus (CoV) / Mpro	2Q 6D	B	Avian CoV / Mpro	1W SU	F	<i>Moarella thermoacetica</i> / Selenocysteine-specific elongation factor
2Q 6D	B	Avian CoV / Mpro	6JI J	C	Murine CoV / Replicative polyprotein 1ab	2L NB	A	Human / Z-DNA-binding protein 1
6JI J	C	Murine CoV / Replicative polyprotein 1ab	5Z QG	A	Porcine epidemic diarrhea virus (CoV) / Non-structural protein	4Z DT	D	<i>Schizosaccharomyces pombe</i> / Structure-specific endonuclease subunit slx4
5Z QG	A	Porcine epidemic diarrhea virus (CoV) / Non-structural protein	2Q 6F	A	Avian CoV / Mpro			
2Q 6F	A	Avian CoV / Mpro	3D 23	B	Human CoV HKU1 / Mpro			
3D 23	B	Human CoV HKU1 / M ^{pro}	2LI Z	A	SARS CoV (domain 3) / Mpro			
2LI Z	A	SARS CoV (domain 3) / Mpro	3E BN	D	SARS CoV (domain 3) / Replicase polyprotein 1ab			
3E BN	D	SARS CoV (domain 3) / Replicase polyprotein 1ab	4H AN	A	Human / Galectin-8			

4H AN	A	Human / Galectin-8	2M P3	A	Human / Superoxide dismutase			
2M P3	A	Human / Superoxide dismutase	3K BE	A	<i>Caenorhabditis elegans</i> / Superoxide dismutase			

Table S5: Sequence similarity of template structures to SARS CoV-2 Main protease. Alignments performed and scores calculated using the BLOSUM62 comparison matrix, gap opening penalty of 12, and gap extension penalty of 4. Scores and alignments calculated with the SIM tool¹⁴ available at <https://web.expasy.org/sim/>

Full						Date-Limited						Sequence-Limited					
PDB ID	Chain	Identity ¹	Overlap ²	Score ³	Gap ⁴	PDB ID	Chain	Identity ¹	Overlap ²	Score ³	Gap ⁴	PDB ID	Chain	Identity ¹	Overlap ²	Score ³	Gap ⁴
3SND	A	96.10%	306	1600	0.00%	3SND	A	96.10%	306	1600	0.00%	4HAN	A	23.10%	26	37	0.00%
6YB7	A	100.00%	306	1646	0.00%	2YNA	A	49.20%	309	755	1.90%	2MP3	A	30.80%	26	29	0.00%
2YNA	A	49.20%	309	755	1.90%	4WME	D	49.50%	309	775	1.90%	3KBE	A	53.80%	13	28	0.00%
4WME	D	49.50%	309	775	1.90%	5HYO	A	45.50%	303	653	1.30%	2IJD	A	33.30%	18	31	0.00%
5HYO	A	45.50%	303	653	1.30%	3TLO	A	44.30%	307	624	1.60%	3MMG	A	28.60%	21	26	0.00%
3TLO	A	44.30%	307	624	1.60%	1LVO	B	44.80%	306	626	1.30%	1LVM	A	50.00%	12	32	0.00%
1LVO	B	44.80%	306	626	1.30%	3D23	D	49.20%	303	755	1.00%	1LVM	B	50.00%	12	32	0.00%
3D23	D	49.20%	303	755	1.00%	4ZRO	A	44.20%	303	628	1.30%	5HXF	A	22.70%	44	33	0.00%
4ZRO	A	44.20%	303	628	1.30%	5NH0	B	44.40%	304	619	1.60%	4XLG	B	54.50%	11	31	0.00%
5NH0	B	44.40%	304	619	1.60%	4XFQ	A	45.20%	303	650	1.30%	1WSU	D	37.50%	24	36	0.00%
4XFQ	A	45.20%	303	650	1.30%	2Q6D	B	40.30%	313	520	4.20%	1WSU	F	37.50%	24	36	0.00%
2Q6D	B	40.30%	313	520	4.20%	6JIJ	C	50.00%	306	750	1.60%	2LNB	A	25.00%	32	26	0.00%
6JIJ	C	50.00%	306	750	1.60%	5ZQG	A	44.90%	303	641	1.30%	4ZDT	D	30.00%	10	24	0.00%
5ZQG	A	44.90%	303	641	1.30%	2Q6F	A	40.30%	313	520	4.20%						
2Q6F	A	40.30%	313	520	4.20%	3D23	B	49.20%	303	755	1.00%						
3D23	B	49.20%	303	755	1.00%	2LIZ	A	96.70%	120	610	0.00%						
2LIZ	A	96.70%	120	610	0.00%	3EBN	D	96.60%	118	599	0.00%						
3EBN	D	96.60%	118	599	0.00%	4HAN	A	23.10%	26	37	0.00%						
4HAN	A	23.10%	26	37	0.00%	2MP3	A	30.80%	26	29	0.00%						
2MP3	A	30.80%	26	29	0.00%	3KBE	A	53.80%	13	28	0.00%						

¹ Percentage of aligned residues that are identical between reference (PDB: 5R8T) sequence and target sequence.

² Number of residues in the target sequence that are aligned with the reference sequence.

³ The optimal alignment score

⁴ The percentage of residues in the full target sequence that are not included in the alignment.

References

1. Robertson, A. J.; Ying, J.; Bax, A., Four-dimensional NOE-NOE spectroscopy of SARS-CoV-2 Main Protease to facilitate resonance assignment and structural analysis. *Magn. Reson.* **2021**, 2 (1), 129-138.
2. Altincekic, N.; Korn, S. M.; Qureshi, N. S.; Dujardin, M.; Ninot-Pedrosa, M.; Abele, R.; Saad, M. J. A.; Alfano, C.; Almeida, F. C. L.; Alshamleh, I.; de Amorim, G. C.; Anderson, T. K.; Anobom, C. D.; Anorma, C.; Bains, J. K.; Bax, A.; Blackledge, M.; Blechar, J.; Bockmann, A.; Brigandat, L.; Bula, A.; Butikofer, M.; Camacho-Zarco, A. R.; Carlomagno, T.; Caruso, I. P.; Ceylan, B.; Chaikuad, A.; Chu, F. X.; Cole, L.; Crosby, M. G.; de Jesus, V.; Dhamotharan, K.; Felli, I. C.; Ferner, J.; Fleischmann, Y.; Fogeron, M. L.; Fourkiotis, N. K.; Fuks, C.; Furtig, B.; Gallo, A.; Gande, S. L.; Gerez, J. A.; Ghosh, D.; Gomes-Neto, F.; Gorbatyuk, O.; Guseva, S.; Hacker, C.; Hafner, S.; Hao, B.; Hargittay, B.; Henzler-Wildman, K.; Hoch, J. C.; Hohmann, K. F.; Hutchison, M. T.; Jaudzems, K.; Jovic, K.; Kaderli, J.; Kalnins, G.; Kanepe, I.; Kirchdoerfer, R. N.; Kirkpatrick, J.; Knapp, S.; Krishnathas, R.; Kutz, F.; zur Lage, S.; Lambertz, R.; Lang, A.; Laurens, D.; Lecoq, L.; Linhard, V.; Lohr, F.; Malki, A.; Bessa, L. M.; Martin, R. W.; Matzel, T.; Maurin, D.; McNutt, S. W.; Mebus-Antunes, N. C.; Meier, B. H.; Meiser, N.; Mompean, M.; Monaca, E.; Montserret, R.; Perez, L. M.; Moser, C.; Muhle-Goll, C.; Neves-Martins, T. C.; Ni, X. M. N.; Norton-Baker, B.; Pierattelli, R.; Pontoriero, L.; Pustovalova, Y.; Ohlenschlager, O.; Orts, J.; Da Poian, A. T.; Pyper, D. J.; Richter, C.; Riek, R.; Rienstra, C. M.; Robertson, A.; Pinheiro, A. S.; Sabbatella, R.; Salvi, N.; Saxena, K.; Schulte, L.; Schiavina, M.; Schwalbe, H.; Silber, M.; Almeida, M. D.; Sprague-Piercy, M. A.; Spyroulias, G. A.; Sreeramulu, S.; Tants, J. N.; Tars, K.; Torres, F.; Tows, S.; Trevino, M. A.; Trucks, S.; Tsika, A. C.; Varga, K.; Wang, Y.; Weber, M. E.; Weigand, J. E.; Wiedemann, C.; Wirmer-Bartoschek, J.; Martin, M. A. W.; Zehnder, J.; Hengesbach, M.; Schlundt, A., Large-Scale Recombinant Production of the SARS-CoV-2 Proteome for High-Throughput and Structural Biology Applications. *Frontiers in Molecular Biosciences* **2021**, 8.
3. Smith, T. F.; Waterman, M. S., Identification of common molecular subsequences. *J. Mol. Biol.* **1981**, 147 (1), 195-197.
4. Henikoff, S.; Henikoff, J. G., Amino-acid substitution matrices from protein blocks. *Proc. Natl. Acad. Sci. U. S. A.* **1992**, 89 (22), 10915-10919.
5. Altschul, S. F.; Erickson, B. W., Optimal sequence alignment using affine gap costs. *Bulletin of Mathematical Biology* **1986**, 48 (5-6), 603-616.
6. Salzmann, M.; Wider, G.; Pervushin, K.; Senn, H.; Wuthrich, K., TROSY-type triple-resonance experiments for sequential NMR assignments of large proteins. *J. Am. Chem. Soc.* **1999**, 121 (4), 844-848.
7. Fitzkee, N. C.; Bax, A., Facile measurement of H-1-N-15 residual dipolar couplings in larger perdeuterated proteins. *J. Biomol. NMR* **2010**, 48 (2), 65-70.
8. Grzesiek, S.; Bax, A., The Importance of Not Saturating H₂O in Protein NMR. Application to Sensitivity Enhancement and NOE Measurement. *J. Am. Chem. Soc.* **1993**, 115 (26), 12593-12594.
9. Emsley, L.; Bodenhausen, G., Gaussian Pulse Cascades - New Analytical Functions for Rectangular Selective Inversion and in-Phase Excitation in Nmr. *Chem. Phys. Lett.* **1990**, 165 (6), 469-476.
10. Kay, L. E.; Keifer, P.; Saarinen, T., Pure Absorption Gradient Enhanced Heteronuclear Single Quantum Correlation Spectroscopy with Improved Sensitivity. *J. Am. Chem. Soc.* **1992**, 114, 10663-10665.
11. Hwang, T. L.; van Zijl, P. C. M.; Garwood, M., Fast broadband inversion by adiabatic pulses. *J. Magn. Reson.* **1998**, 133 (1), 200-203.
12. Delaglio, F.; Grzesiek, S.; Vuister, G. W.; Zhu, G.; Pfeifer, J.; Bax, A., NMRpipe - a multidimensional spectral processing system based on Unix pipes. *J. Biomol. NMR* **1995**, 6 (3), 277-293.
13. Williams, C. J.; Headd, J. J.; Moriarty, N. W.; Prisant, M. G.; Videau, L. L.; Deis, L. N.; Verma, V.; Keedy, D. A.; Hintze, B. J.; Chen, V. B.; Jain, S.; Lewis, S. M.; Arendall, W. B., 3rd; Snoeyink, J.; Adams, P.

- D.; Lovell, S. C.; Richardson, J. S.; Richardson, D. C., MolProbity: More and better reference data for improved all-atom structure validation. *Protein Sci.* **2018**, *27* (1), 293-315.
14. Huang, X.; Miller, W., A time-efficient, linear-space local similarity algorithm. *Adv. Appl. Math.* **1991**, *12* (3), 337–357.